International Journal of Greenhouse Gas Control 109 (2021) 103363

Contents lists available at ScienceDirect

International Journal of Greenhouse Gas Control

journal homepage: www.elsevier.com/locate/ijggc

Time-lapse imaging of CO_2 migration within near-surface sediments during a controlled sub-seabed release experiment

Ben Roche [a,*], Jonathan M. Bull [a], Hector Marin-Moreno [b,c], Timothy G. Leighton [d], Ismael H. Falcon-Suarez [b], Madeleine Tholen [a], Paul R. White [d], Giuseppe Provenzano [a], Anna Lichtschlag [b], Jianghui Li [d], Michael Faggetter [a]

[a] School of Ocean and Earth Science, National Oceanography Centre Southampton, University of Southampton Waterfront Campus, European Way, Southampton SO14 3ZH, UK
[b] National Oceanography Centre, University of Southampton Waterfront Campus, European Way, Southampton SO14 3ZH, UK
[c] Norwegian Geotechnical Institute, PB 3930 Ullevål Stadion, NO-08906 Oslo, Norway
[d] Institute of Sound and Vibration Research, University of Southampton, Southampton SO17 1BJ, UK

ARTICLE INFO

Keywords:
CO_2 injection
Time lapse seismic imaging
Gas migration
Carbon capture and storage
Fracture propagation

ABSTRACT

The ability to detect and monitor any escape of carbon dioxide (CO_2) from sub-seafloor CO_2 storage reservoirs is essential for public acceptance of carbon capture and storage (CCS) as a climate change mitigation strategy. Here, we use repeated high-resolution seismic reflection surveys acquired using a chirp profiler mounted on an autonomous underwater vehicle (AUV), to image CO_2 gas released into shallow sub-surface sediments above a potential CCS storage site at 120 m water depth in the North Sea. Observations of temporal changes in seismic reflectivity, attenuation, unit thickness and the bulk permeability of sediment were used to develop a four-stage model of the evolution of gas migration in shallow marine sediments: Proto-migration, Immature Migration, Mature Migration, and Pathway Closure. Bubble flow was initially enabled through the propagation of stable fractures but, over time, transitioned to dynamic fractures with an associated step change in permeability. Once the gas injection rate exceeded the rate at which gas could escape the coarser sediments overlying the injection point, gas began to pool along a grain size boundary. This enhanced understanding of the migration of free gas in near-surface sediments will help improve methods of detection and quantification of gas in subsurface marine sediments.

1. Introduction

Since the industrial revolution, the concentration of CO_2 in the atmosphere has risen from 277 parts per million (ppm) to a current level of $>$ 410 ppm (Friedlingstein et al., 2019). This rise has been directly linked to anthropogenic sources such as the burning of fossil fuels, the manufacture of cement, and changing land uses (Friedlingstein et al., 2019). The increased level of atmospheric CO_2 has resulted in a rise in the global mean surface temperature of 1 °C (IPCC, 2018). Global warming has already had a severe negative effect on the environment, leading the United Nations Framework Convention on Climate Change (United Nations, 2015) to agree on a strategic plan to stop the global mean temperature from rising more than 2°C above the pre-industrial level (IPCC, 2014).

The large-scale adoption of Carbon dioxide Capture and Storage (CCS) has been identified as a key factor for reducing anthropogenic greenhouse gas emissions to reach climate goals (IPCC 2014). During CCS activities, CO_2 gas produced during industrial processes is captured and stored in appropriate geological reservoirs deep beneath the surface to mitigate the potential greenhouse effects. Compared to other strategies, such as enhanced energy efficiency and the use of renewable energy sources, the crucial benefit of CCS lies in its potential to reduce (in a significant, timely, and cost-effective way) the CO_2 emissions, by utilizing existing infrastructure from oil and gas production (IPCC, 2005). Depleted hydrocarbon fields in the North Sea are prime candidates for CCS storage with the potential to hold 475–570 Mt of CO_2 (Strachan et al., 2011). Several successful demonstration projects have already provided confidence in the performance of offshore gas injection and storage; K12-B (North Sea, Netherlands), Sleipner (North Sea, Norway), and Snøhvit (Barents Sea, Norway) (Vandeweijer et al., 2011; Hansen

* Corresponding author.
E-mail address: Br4g13@soton.ac.uk (B. Roche).

https://doi.org/10.1016/j.ijggc.2021.103363
Received 23 June 2020; Received in revised form 6 May 2021; Accepted 17 May 2021
Available online 1 June 2021

et al., 2013; Van der Meer, 2013; Furre et al., al.,2017; Ringrose and Meckel, 2019). However, robust strategies for leak detection and management are still in their infancy despite being a regulatory requirement to comply with international marine legislation (e.g., EU CCS Directive, London Protocol, OSPAR) and must be advanced to make CCS a safe and reliable strategy for the long-term mitigation of atmospheric CO_2 increase.

While CO_2 escape from a CCS site is unlikely (IEAGHG, 2013), risks can broadly be categorised into two types: i) injection facility failure and ii) seal failure. Injection facility failure would occur close to the seabed and include faulty pipelines, wellheads, or injection wells within the subsurface, and can be considered part of the standard operating risk of offshore oil and gas facilities. Seal failure would occur at much greater depth and is most likely caused by either inadequately secured abandoned wells, or previously undetected/newly formed small-scale stress-induced fractures increasing permeability across a cap rock. These create fluid pathways for injected gas to escape back to the surface. While failure at injection facilities would typically be detected very quickly (if not immediately), failure across a seal could take several days or even years to have an effect on the seabed e.g. detection of bubble plumes in the water column, changes in the pH of bottom waters or changes in the distribution of benthic fauna and flora. Monitoring sub-surface integrity using sub-bottom methods would allow anomalies to be determined earlier than seabed observation techniques (Jenkins et al., 2012; Dean et al., 2020).

Therefore, to enable the large-scale implementation of CCS, a greater understanding of the fate of injected CO_2 in the subsurface is crucial, particularly regarding its migration in the uppermost sedimentary succession. Our understanding of newly self-established fluid flow features (gas conduits to the seabed), and their effect on the surrounding sediment conditions our ability to detect CCS leakage and ameliorate any potential environmental impacts. More broadly, such work will enhance our understanding of processes operating in sub-seabed natural CO_2 and CH_4 (methane) seeps that are found around the globe (Dlugokencky et al., 2011; Ruppel and Kessler, 2017).

Several international projects such as ECO_2 (Sub-seabed CO_2 Storage: Impact on Marine Ecosystems), QICS (Quantifying and Monitoring Potential Ecosystem Impacts of Geological Carbon Storage), and ETI MMV (Energy Technologies Institute Measurement, Monitoring, and Verification of CO_2 Storage) have contributed to improving our ability to detect potential leaks at the seafloor and the impact of the CO_2 leakage on marine ecosystems (Dean et al., 2020; Blackford et al., 2014;

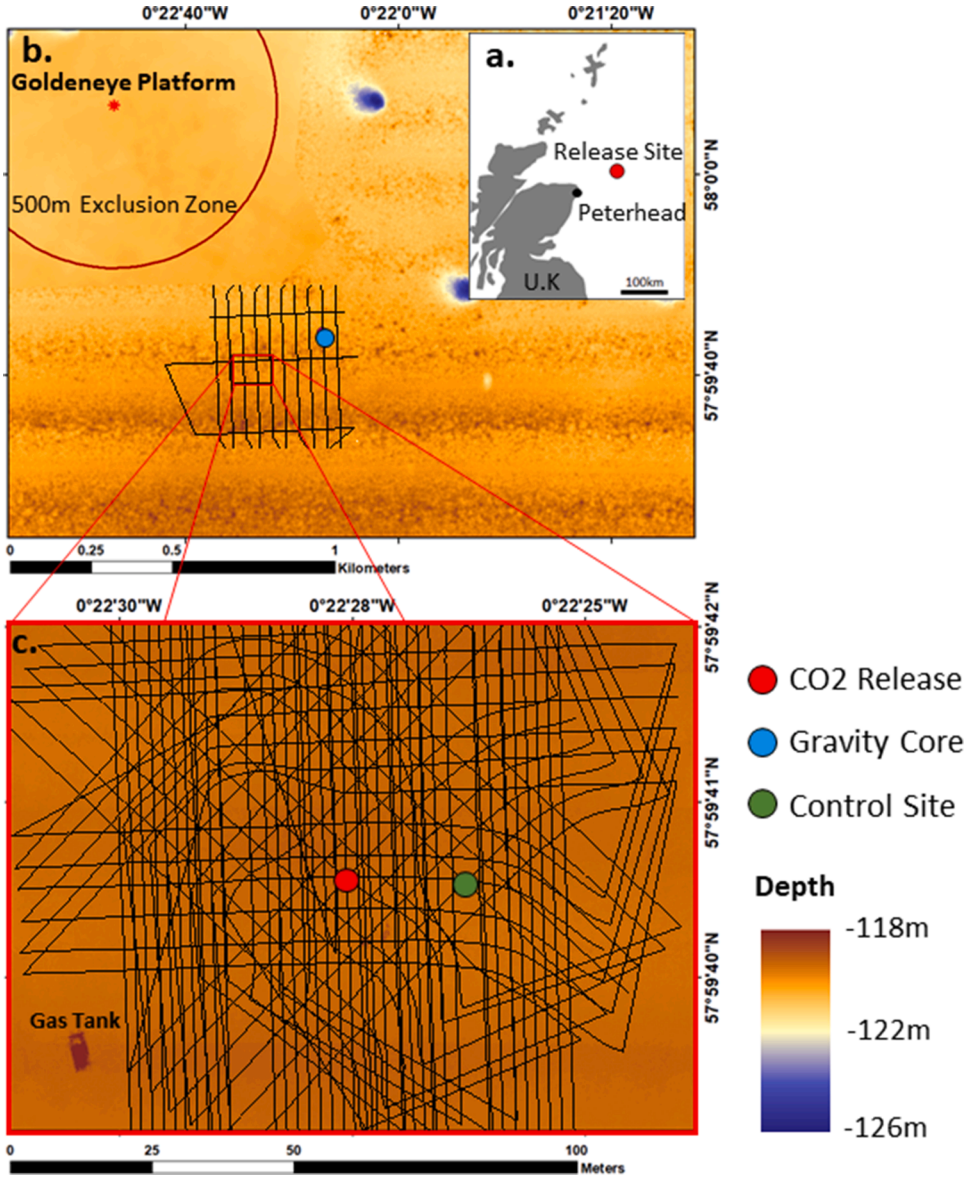

Fig. 1. Location of the CO_2 controlled-release site and survey configuration (a) The Goldeneye complex located 100 km northeast of Peterhead. (b) Position of pre-release autonomous underwater vehicle-mounted chirp profiles (black lines) in relation to the Goldeneye platform and gravity core position (in purple). (c) Positions of the syn- and post-release AUV chirp profiles. The epicentre of the CO_2 release (red dot), chirp profile is shown in Fig. 4, and the location of the control site (green dot) is shown together with bathymetry.

Blackford et al., 2017; Jones et al., 2015; Taylor et al., 2015). The STEMM-CCS (Strategies for Environmental Monitoring of Marine Carbon Capture and Storage) project was subsequently established with the overall aim of converting this information into quantified knowledge that would enable cost-effective monitoring in the marine environment for realistic CO_2 leak scenarios.

Central to the STEMM-CCS project was a controlled CO_2 release experiment in the North Sea (Fig. 1) designed to simulate a CO_2 leak from a sub-seabed CCS site, to demonstrate and evaluate new approaches for detecting or quantifying this release (Flohr et al., 2021). We use AUV-mounted 2D seismic reflection chirp data collected before, during, and after the release, alongside detailed core analysis, in order to create a time-lapse record of the CO_2 migration. This paper describes in detail the evolution of gas migration pathways, culminating in the formation of seismic chimneys, with a particular focus on constraining the primary mechanisms (stable and dynamic fracture propagation) by which gas migrates within the near-surface over time. Using seismic time lapse imaging, we examine the development of enhanced reflectors, shadowing, as well as variations in attenuation, RMS amplitude, and unit thickness.

2. Gas migration in near-surface sediments

The upward migration of gases in the form of bubbles through near-surface, unconsolidated sediment is a rapid process, which allows the gases to bypass oxidation or absorption processes (Knittel and Boetius, 2009). While our study is concerned with CO_2 gas, most of the principles are equally applicable to other gases including methane (CH_4), another greenhouse gas (Landrø et al., 2019).

In order to understand the migration of gas through sediment, we first consider the migration history of a single bubble, from its nucleation to its escape into the water column. A bubble is a pocket of gas, in our case CO_2, surrounded by a liquid host medium. While traditionally this term is applied to pockets of air in the water column it can also be applied to pockets of gas in water saturated sediment. In the interests of clarity, we will refer to pockets of CO_2 gas in the water column as simply "bubbles", and pockets of CO_2 gas in the sediment as "bubble fractures" and "capillary CO_2". In a typical near-surface marine sediment, the pores between grains are saturated with water. The introduction of gas, for example from an underlying fracture, slowly invades the surrounding pores, displacing the water. This intrusion can occur either by capillary invasion or by fracture opening. In capillary invasion, the gas forces its way into a new pore if the capillary pressure (the difference between gas pressure and water pressure) is larger than the capillary entry pressure. This is more common in coarser-grained sediment and occurs without movement of the surrounding grains. The capillary invasion continues in an outward direction from the point of injection (generally upwards) with gas moving from pore to pore, often replaced by the surrounding water, thus dispersing the gas without the creation of a bubble fracture (Jain and Juanes, 2009). Alternatively, intrusion may occur via fracture opening, whereby the gas within a pore naturally exerts a net pressure on the surrounding grains. As the two fluids do not mix, this pressure difference does not dissipate and leads to the rearrangement of surrounding grains, preferentially fracturing the sediment (Boudreau et al., 2005; Jain and Juanes, 2009; Katsman et al., 2013). This fracture opening is the initial nucleation of a bubble in sediment, as the gas forms its own "cavity" within the surrounding medium.

After nucleation, a bubble fracture exists in a heterogeneous pressure field that increases with depth, resulting in a pressure difference between the top and the bottom of the bubble fracture. This gradient, combined with the difference in density between the bubble fracture itself and the surrounding medium, creates a pseudo-buoyancy force (Boudreau et al., 2005; Algar et al., 2011). If the bubble fracture is large enough, this force allows the fracture to rise upwards through the sediment, the weaker (less cohesive) the sediment, the smaller the fracture needs to be. The upwards force exerted by the bubble fracture on the host medium (the surrounding sediment) depends on the volume of the body, not its shape, and does not depend on its vertical extent, provided the above assumptions hold true and that the body moves coherently as a single entity. Real bubble fractures in marine sediment might easily depart from this latter restriction, through deformation, fragmentation, and coalescence. Furthermore, the properties of the sediment can greatly change the resistive forces that oppose this rise (such as sediment cohesion, and the weight of the gas /vapour mixture itself) and affect bubble fragmentation and coalescence, and how these forces change in time.

The nature of bubble fracture propagation in soft sediment is commonly described via linear elastic fracture mechanics (LEFM) where the bubble can be imagined as a very thin oblate spheroid, the long axis orientated vertically, forming what is known as a "penny-shaped" crack in the sediment (Boudreau et al., 2005; Algar et al., 2011; Boudreau 2012). From here the bubble fracture may propagate through either stable or dynamic fracture propagation. We will first describe stable fracture propagation, a fundamental process that is most in need of refinement.

2.1. Stable propagation

The most prominent application of LEFM to stable fracture propagation was first presented by Algar et al. (2011). They describe how the interior gas of the bubble fracture exerts an outward pressure on the crack walls/sediment with the resulting tensile stresses concentrated at the upper crack tip (Algar et al., 2011) and is characterised by the stress intensity factor K_1;

$$K_1 = \frac{2}{\pi}\sigma\sqrt{a\pi} \tag{1}$$

where σ is the internal bubble pressure in excess of the ambient pressure (i.e., the applied stress), and a is the half major axis of the crack/bubble. If the stress intensity factor K_1 is greater than the stress the material can take before tensile failure, the fracture toughness of the sediment K_{ic}, the fracture will propagate (Algar et al., 2011).

As the fracture expands upwards, the length of the crack/bubble increases, and the pressure difference between the tip and the tail of the crack eventually disappears and the internal bubble pressure equals the compressive stresses of the surrounding medium (σ=0) (Algar et al., 2011). This results in a lower stress intensity factor ($K_1 < K_{ic}$) at the top of the crack, halting propagation. As a result of heterogeneous stress field, the compressive forces at the crack tail force it to close, morphing the bubble into an inverted teardrop shape. The sealing up of the crack behind the rising bubble fracture decreases the crack length, raising the internal bubble pressure and reverting it to its original condition, which restarts the fracture propagation process slightly higher up. The cycle repeats, leading to the bubble fracture rising upwards through the sediment in an alternating sequence of elastic expansion and fracturing, which is commonly referred to as "stable fracture propagation" (Boudreau et al., 2005; Algar et al., 2011; Katsman et al., 2013; Katsman 2019). The rise speed of a bubble fracture is regulated by the period of this cycle, i.e. the length of time between a tip opening and the tail closing, which depends upon the elasticity of the sediment (Boudreau et al., 2005; Boudreau 2012; Algar et al., 2011). The minimum critical size at which a bubble fracture will begin to rise a_r is determined by the properties of the surrounding sediment, and can be calculated as follows (Barry et al., 2012; Johnson et al., 2012; Johnson et al., 2002):

$$a_r = \left(\frac{3K_{ic}\sqrt{\pi}}{10g[\rho_s(1-\varphi)+\rho_w\varphi]}\right)^{2/3} \tag{2}$$

where ρ_s is the density of the solid grains, ρ_w is the density of water, g is the acceleration due to gravity and φ is the porosity of the sediment (Boudreau 2012; Algar et al., 2011).

While Algar et al. (2011) model is the most comprehensive theory on

the concept of stable fracture propagation, with good experimental correlation, there are a number of oversimplifications. Perhaps the most important is that the theory is based on the concept that the sediment acts as a single entity. Even for the most cohesive sediment this is not true. Furthermore, to apply a straightforward adaptation of standard analyses (Westergaard 1939; Irwin 1957) for crack propagation in solids, Algar et al. (2011) restricted their consideration to cases where they could argue that the solid around the bubble fracture was 'dry'. Anderson et al. (1998) characterised bubbles propagating via fracture mechanics (Type 3 bubbles) as a gas pocket formed by the displacement of both sediment and liquid. If we acknowledge a bubble consists of both a pocket of gas and its surroundings (Leighton 1996), then the characteristic properties of the bubble fracture (the way its wall moves in response to external drivers; mass transfer across its wall etc.) will depend on both the gas and the surrounding medium. If there is a space between sediment grains that contains an area of gas and an area of liquid water (as opposed to vapour), the interface between the water and the gas forms part of the bubble wall. This clarification highlights the need to have precise definitions, for what is meant by 'dry' formation of new space between the grains, the definition of the bubble wall (the interface between a finite, contiguous but enclosed volume of gas and/or vapour, and the surrounding liquid (and optionally solid) medium or mixture). The specification that the volume is enclosed means that gas cannot escape into dry channels between grains if the gas pressure increases marginally.

Such a concept has a wet interface across the bubble fracture wall, providing a Laplace pressure. We are thus able to relax the concept of dry fractures according to Algar et al. (2011) by assuming that the bubble wall will "always" be in contact with water and incorporating the associated capillary pressure into the definition of the stress intensity factor, amending Eq. (1) to the form:

$$K_1 = \frac{2}{\pi}\sigma\left(1-\frac{\tau}{\sigma}\left(\frac{1}{a}+\frac{1}{b}\right)\right)\sqrt{a\pi} = \frac{2\sqrt{a}}{\sqrt{\pi}}\left(\sigma-\tau\left(\frac{1}{a}+\frac{1}{b}\right)\right) \quad (3)$$

where σ is the internal bubble pressure in excess of the ambient pressure, b is the half minor axis, and τ is the surface tension characterising the interface between the gas and the liquid. We must assume the fracture has an aspect ratio $b/a \ll 1$ as the concept is only valid for non-spherical bubbles. Note that the above revision does not affect the critical crack size in Eq. (2) as this depends on the fracture toughness of the sediment K_{ic}, and not the stress intensity factor of the crack/bubble tip K_1.

Although we suggest further work is needed to refine this model, particularly to take into account sediment properties and (most importantly) the wetness of a bubble fracture wall, the mechanism proposed by Algar et al. (2011) of stable fracture propagation is still our best working model, showing good agreement with field data.

In the marine environment gas originating deep below the seabed is subject to a large overburden pressure. This high-pressure causes bubble fractures to ascend via stable propagation with minimal absorption into the surrounding water, as previously mentioned. The gas will continue to rise until the net solute supply through its surface drops to zero, creating a so-called "gas horizon" (i.e., a surface across which bubble ascension stops) (Sirhan et al., 2019), which can, in turn, create a secondary gas reservoir. This horizon is commonly related to variations in grain size, which are typically stratified in marine settings. Thereafter, to reach the water column, the gas must be mobilized by either i) decreasing hydrostatic pressure (commonly due to tidal variations), altering the depth of the gas horizon to some point above the seabed, allowing stable propagation to resume (Sirhan et al., 2019; Katsman 2019); or ii) the formation of fluid conduits connecting the gas horizon to the seabed, allowing gas to rise via dynamic propagation. It should be noted that for the STEMM-CCS release experiment we introduced gas above some naturally-occurring gas horizons.

2.2. Dynamic propagation

Dynamic bubble fracture propagation occurs either when a crack exceeds a certain critical length (e.g., due to the crack propagating into some pre-existing cavity) or due to rapid variation in loading on the surface of the bubble (e.g., due to internal waves in the overlying water column), which is characterized by a continuously increasing stress intensity factor K_1 at the tip of the bubble (Sirhan et al., 2019). The crack propagates rapidly forming a long-elongated fracture towards the seabed. The internal gas quickly rises upwards, potentially into the water column, reducing the internal pressure and allowing the fracture to close (Katsman 2019).

The passage of a bubble fracture through sediment will momentarily weaken the strength of the sediment left in its wake as the grains are temporarily displaced from their originally stable position. As a result, the buoyant forces required for a subsequent bubble fracture to rise do not need to do as much work to displace the grains. This weakening of sediment facilitates the propagation route for subsequent bubbles fractures. Initially, these conduits are narrow and easily blocked off by external pressure changes condensing/strengthening the sediment but as time goes on the longer-lasting of these channels become more permanent. The continuous passage of bubble fractures through the same area extends the sediment weakening to a larger area (centimetre scale), enhancing the fluid (gas) conductivity through the sediment. Eventually, bubble fractures begin to connect together (i.e., extending crack length beyond the critical length a_r) leading to a transition from stable to dynamic propagation (Katsman 2019; Sirhan et al., 2019). Over time, these dynamic pathways slowly become connected forming open conduits through which gas can pass virtually unrestricted for as long as the gas flux is sufficient to maintain the internal pressure of the fracture, preventing pathway closure. This can be considered the creation of a small-scale chimney structure.

2.3. The acoustics of gas bearing sediments

The use of ultra-high-frequency (UHF; kHz range) marine seismic reflection to create time lapse studies of marine sediment is still relatively rare (Vardy et al., 2017), mainly due to the demanding positional requirements. However, Faggetter et al. (2020) demonstrate that with high-accuracy positioning and careful processing it is possible to image tidally-influenced methane migration on a decimetre-scale between repeat chirp surveys within shallow marine sediments. Time-lapse imaging of CO_2 migration using chirp profilers was completed as part of the QICS project during which CO_2 was injected 10 m below the seabed of a shallow loch in western Scotland (Cevatoglu et al., 2015). The QICS experiment was completed at ~10 m water depth, so its results are of limited use for deeper marine settings that are of greater interest to the CCS community. Landrø et al. (2019) used time-lapse seismic reflection data in a deep marine (>100 m water depth) setting to study the migration of gas resulting from a hydrocarbon exploration well blowout in the North Sea, at 4700 m depth. They found that most of the leaked gas became trapped in shallow sand layers within the first 1000 m of sediment beneath the seabed indicating a possible tendency for gas flow to become static after an extended period (~20 years). However, they were unable to focus on the small-scale alterations in the near-surface given the nature of their survey equipment. The STEMM-CCS study is thus in a unique position to examine the initial migration of gas through the near-surface and the formation of chimney structures in a deep (>100 m water depth) marine environment with the use of pseudo-3D time lapse 2D seismic reflection chirp data.

3. STEMM-CCS controlled release experiment

The STEMM-CCS controlled CO_2 release experiment was conducted in the central North Sea near the Goldeneye platform (Fig. 1a), approximately 100 km northeast of Peterhead, Scotland, at ~120 m

water depth (Shell 2018). The area has been identified as a potential CCS site (Dean and Tucker 2017).

For the experiment, a curved pipe was pushed into the unconsolidated marine sediments with the leading end terminating ~3 m below the seabed (Flohr et al., 2021). The surface end of the pipe was connected to a specially built gas container located 80 m east of the pipe, that contained 3 tonnes of CO_2 gas and additional gas tracers (positions shown in Fig. 1c). The subsurface end of the pipe comprised a 460 mm long sintered stainless-steel diffuser, with a pore size of 9 μm, through which the gas was injected into the sediment. The pipe had an upward curve to ensure that the sediment directly above the release point was undisturbed by its emplacement and migration pathways could develop naturally.

During the main phase of the experiment, gas was released into the sediment via the injection pipe. The injection rate was 6 kg/day on day 0 (D 0; Table 1) and almost immediately after injection began sporadic gas bubbles were visible along the seabed above the release site and within hours small seeps (the continuous release of gas bubbles from a fixed position) began to form. The injection rate was progressively stepped up (see Fig. 2 and Table 1) to a maximum of 143 kg/day ($D + 8$) before gas release was stopped on Day + 11.

A large number of techniques were deployed to detect and monitor the escaping CO_2 in the subsurface sediments and the overlying water column, including geochemical, optical, passive acoustic, and seismic reflection profiling. This paper will examine the 2D seismic reflection chirp data collected before (D-13), during ($D + 3$, $D + 6$, $D + 9$), and after ($D + 16$) injection, alongside a gravity core collected prior to release, in order to assess the spatial and temporal propagation mechanism of CO_2 in the subsurface. Full details on the STEMM-CCS experiment are provided in Flohr et al. (2021).

3.1. Subsurface structure of release site

Pre-release surveys of the release site identified 6 seismic horizons throughout the study area (Fig. 3a). Beneath the high amplitude, continuous, undulating seabed, Unit 1, identified as the Witch member (Stoker, 1985), is a reflection free unit 2–3 ms Two Way Time (TWT) thick unit composed of moderately sorted sandy and silty muds, deposited during Marine Isotope Stages (MIS) 1–2 (Fig. 3b; Stoker et al., 2011). It is separated from Unit 2, identified as the Fladen member, a reflection free zone 3–4 ms TWT thick composed of moderately sorted pebbly, sandy, and silty muds deposited in a glaciomarine environment (Böttner et al., 2019) by Horizon 2, a weak continuous subparallel reflector. Horizon 3 indicates the base of the Fladen member and is a sub parallel high amplitude continuous reflector. The underlying Horizons 4–6 are high amplitude reflectors with significant topography, varying in depth 1–4 m throughout the release site. The 2D seismic reflection chirp data were tied with gravity core GC06 (Fig. 1b). The majority of the core is composed of homogenous silty/sandy mud and clay with high-water content, but with sparse shell fragments and small pebbles at 3 m below the seafloor (mbsf), and a coarsening in grain size to sand at c. 3.4 – 4.4 mbsf. (Fig. 3b). This coarsening in grain size is likely to reflect the gradational contact between the Witch and Fladen members. The changing grain size is reflected in the variation in the velocity, density, and impedance plots in Fig. 3b. Overall Fig. 3b demonstrates evidence for a change from heterogeneous to homogeneous sediment with increasing depth within the Witch member at 1.5 m and a gradational contact between the Witch and Fladen members at 3.4 mbsf (Horizon 2).

Table 1
Date of acquisition of AUV-mounted chirp seismic reflection surveys with corresponding gas injection rate.

Date /	Time	Days since release (D)	Event
28/04/19	**~13:00**	+13	**Pre-Release Survey (0 kg/day)**
11/05/19	15:27	0	Gas Injection Start 6 kg/day
14/05/19	**~07:00**	**+3**	**Syn-Release Survey 1 (6 kg/day)**
14/05/19	15:27	+3	Gas Injection Increase 14 kg/day
15/05/19	06:48	+4	Gas Injection Increase 29 kg/day
17/05/19	**~07:30**	**+6**	**Syn-Release Survey 2 (29 kg/day)**
17/05/19	16:54	+6	Gas Injection Increase 86 kg/day
19/05/19	15:50	+8	Gas Injection Increase 143 kg/day
20/05/19	**~08:00**	**+9**	**Syn-Release Survey 3 (143 kg/day)**
22/05/19	11:17	+11	Gas Injection stopped
27/05/19	**~07:30**	**+16**	**Post-Release Survey (0 kg/day)**

3.2. Subsurface infrastructure

The injection pipe (Fig. 4) was clearly visible in multiple seismic reflection profiles throughout the release phase of the experiment, which served as our own method to determine the subsurface position of the pipe. As visible in Fig. 4b, the deepest part of the carbon steel pipe approximately two-thirds along its length is located at 4 ms TWT (~4 m) beneath the seabed while the release point is at 3 ms TWT (~3 m) beneath the seabed. This is an important observation as it allows us to pinpoint the exact location of the gas release, within the Fladen member, just below the Witch member lower boundary (Fig. 3).

4. Methodology

4.1. 2D seismic reflection chirp data acquisition

Five high resolution, closely spaced 2D seismic reflection chirp surveys were completed so that gas migration in the sub-surface could be understood: one pre-release, three syn-release, and one post-release (Fig. 2; Table 1). The chirp system was integrated on a GAVIA Autonomous Underwater Vehicle (AUV) which followed pre-programmed routes at either 7.5 or 2.0 m above the seabed. The single channel sub-bottom profiler produced a chirp sweep with source frequencies between 14 and 21 kHz. The source sweep durations for the 7.5 m elevation surveys was 5 ms at maximum power, while the 2 m elevation survey used a shorter sweep length of 1 ms with reduced power. Surveys were conducted at 15 pings per second which equates to an average ping spacing of ~7 cm. The data were recorded in both correlated waveform and uncorrelated raw SEGY data format.

The correlated data was processed using the following flow: band-pass filter (13.5–14.0–21.0–22.0 kHz), top mute, time varying gain, static correction using the mean Gavia elevation, trace mixing (3-point moving average), Stolt constant velocity migration (Stolt 1978) of $1483 ms^{-1}$ based on average water column measurements and automatic gain control (1.3 ms length), and finally enveloped. Enveloping the data allows us to view its instantaneous amplitude improving data interpretability and enhance imaging of the gas. The Gavia navigation data were corrected using the ship's Ultra-short baseline acoustic positioning system. Time-lapse chirp data were static-corrected so that the two-way-time to the seabed was consistent with bathymetry data collected during the cruise, and lateral drift corrected by using the position of static seabed infrastructure.

The pre-release, pre-installation survey (Fig. 1b and Fig. 5a) provided a reference data set against which to benchmark changes in physical properties due to gas injection. As this survey was also used to identify an experiment site where the near-surface sediment (the Witch member) was a uniform thickness it needed to cover a much larger area than later surveys resulting in a sparse survey grid. The on-site grid of

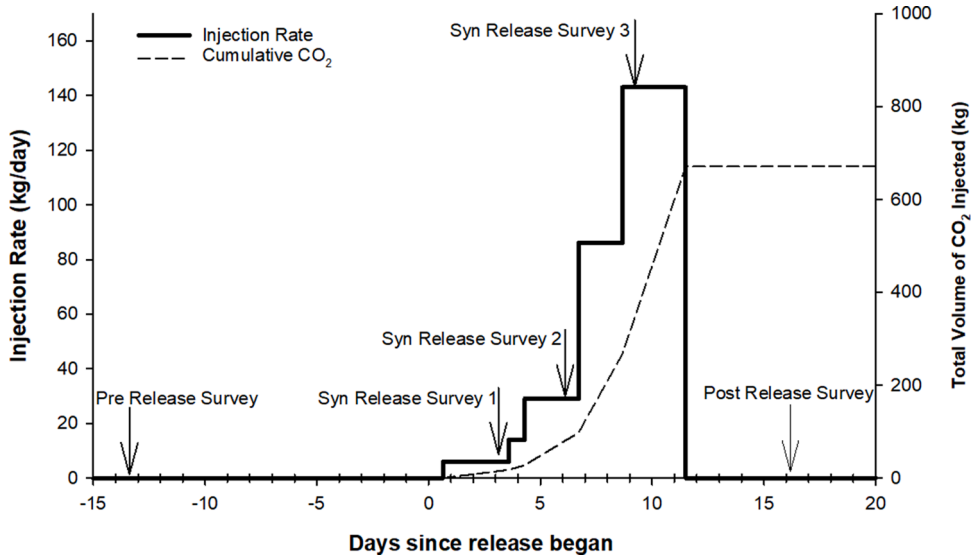

Fig. 2. Gas injection rate and total volume of CO_2 injected during the STEMM-CCS experiment in the North Sea, and the times at which the AUV chirp seismic reflection profiles were acquired.

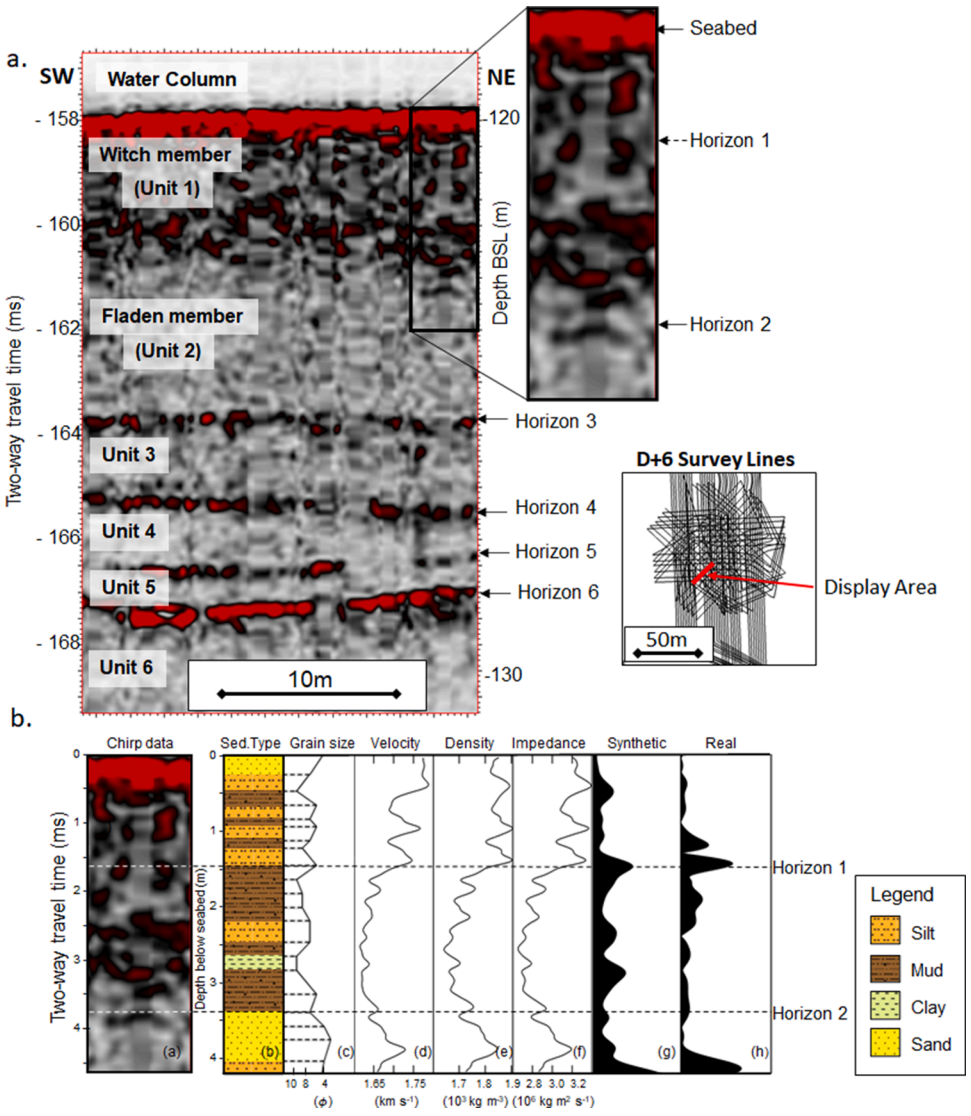

Fig. 3. Sediment stratigraphy at the CO_2 release site. (a) 2D seismic reflection chirp data (instantaneous amplitude) collected on syn-release survey $D + 6$ with units and horizons; enlarged section for comparison with the sediment core data. Data is presented in two-way travel time (TWT) with the equivalent depth below sea level (BSL) provided. (b) Seismo-stratigraphic correlation of gravity core GCO6 with chirp profiler data 500 m from the release site (position shown in Fig. 1b). Sediment interpretation with grain size; P wave velocity, density, calculated impedance with a gaussian-weighted moving average filter of window length 20 samples, synthetic trace based on core data, and real trace from corresponding chirp data. Superimposed on the plots are the interpreted positions of two horizons, one at 1.5 mbsf and one at 3.4 mbsf.

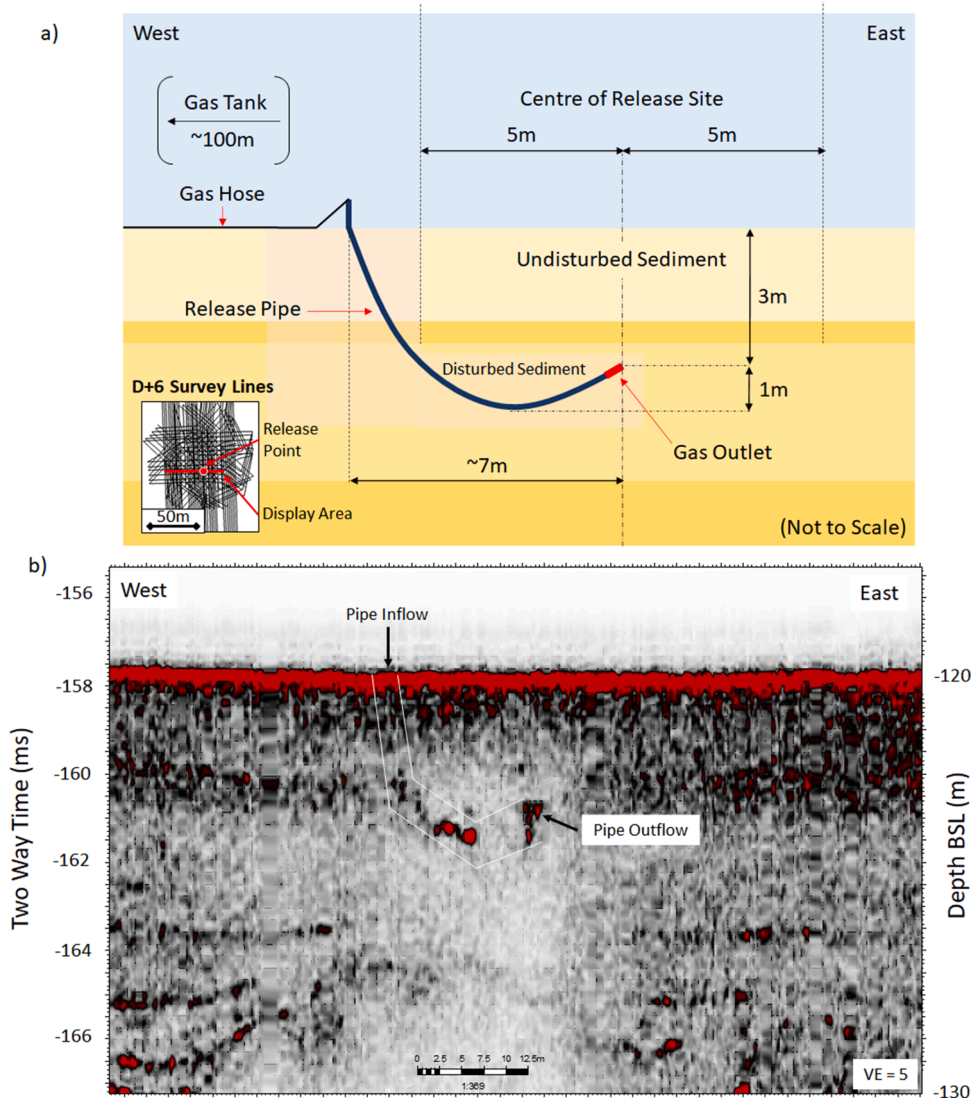

Fig. 4. Geometry of sub-seabed gas release pipe (a) schematic diagram (b) projected onto the 2D seismic reflection chirp data (Instantaneous Amplitude), collected during $D + 3$. The approximate position of the release point (outflow) is visible just beneath the Witch/Fladen member boundary (Horizon 2) at 3 ms beneath the seabed (~3 m). The bright spots in the centre and end of the pipe indicate the accumulation of gas within the pipe and immediately around the diffuser.

lines covered an area of 500 m x 400 m, with a line spacing of 40 m in a north-south direction.

The syn- and post-release surveys were designed to observe the migration of the gas through the sediment while CO_2 was injected at varying rates (Table 1) to determine the longevity of gas in the substrate after the experiment had been concluded. The surveys comprised identical dense grids of lines centred above the epicentre of the release experiment (Fig. 5b-e). Lines were collected at 7.5 m height in a N/S orientation with a 2 m spacing, in a NW/SE and NE/SW with 5 m spacing and at 2 m height in a E/W orientation with a 5 m spacing (Fig. 5b-e).

The data has a vertical resolution of 2 cm, based on a quarter of the dominant chirp wavelength (Kallweit and Wood, 1982). The horizontal resolution (1st Fresnel zone) at a depth of 3 m (i.e. the release point) has a width of 70 cm for the 2 m elevation survey while the 7.5 m elevation survey had an equivalent resolution of 100 cm. Given the close line spacing and interlaced survey pattern, the syn- and post-release surveys are in effect pseudo 3D, making the dataset as a whole a pseudo 4D seismic time-lapse.

4.2. *Gravity core collection and generation of synthetic seismogram*

Gravity cores were collected by the RV Poseidon (POS527), sampling the upper 3–5 m of sediment prior to the CO_2 release. The closest core to the release site, GC06, was analysed for this study (Fig. 1b). The sediment interpretation was based on a modified Udden-Wentworth grain-size scale (Blair and McPherson 1999) and observations of colour change, water content, and fossil content. P-wave velocity, density, and resistivity measurements were made using a Geotek Multi-Sensor Core Logger. From the velocity and density data, a synthetic seismic trace was calculated by convolving the gradient of the smoothed impedance (reflectivity) with the chirp sweep (14 – 21 kHz) Klauder wavelet and enveloping the resulting data for later comparison to the acquired chirp seismic traces.

5. Results and analysis

5.1. *Time lapse imaging of CO2 induced acoustic anomalies*

5.1.1. *Day 3) 6 kg/day release survey*

The seismic reflection data on $D + 3$ (Fig. 6b) appears near identical

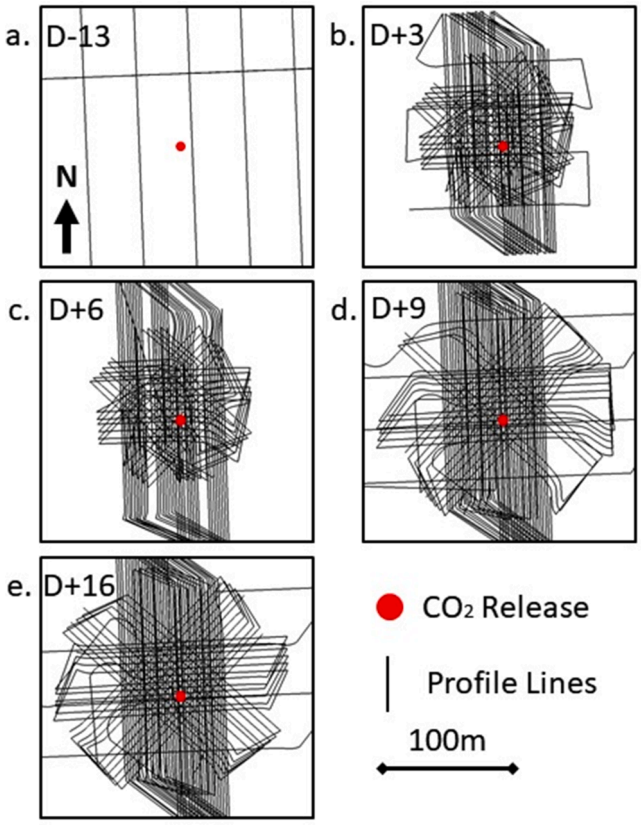

Fig. 5. 2D seismic reflection chirp surveys over the release site collected with an Autonomous Underwater Vehicle. (a) D - 13 CO_2 pre-release profiles; (b) D + 3 syn-release profiles, (c) D + 6 syn-release profiles, (d) D + 9 syn-release profiles, (e) D + 16 post-release profiles. The end of the subsurface pipe is indicated in red.

to the pre-release survey on D-13 (Fig. 6a) with no changes in reflectivity of the sub-surface. The only visual difference relates to the improved quality of data acquisition following a change in survey pattern. Directly above the release point bubbles are visible in the water column, though no clear escape pathways are imaged in the underlying sediment (Fig. 6b).

5.1.2. Day 6) 29 kg/day release survey

Seismic reflection data on D + 6 (Fig. 6c) again appears unchanged compared to the pre-release survey on D-13 (Fig. 6a) as well as the previous syn-release survey on D + 3 (Fig. 6b). The Fladen member appears unchanged. While evidence of bubbles can be seen in the water column in the form of strong reflectors above the seabed there are no clear escape pathways visible in the underlying sediment (Fig. 6c).

5.1.3. Day 9) 143 kg/day release survey

Seismic reflection data on D + 9 shows a strong increase in the reflectivity in the bottom 0.5 ms TWT of the Witch member directly above the release point, extending ~4–5 m in an east west direction and ~7–8 m in a north-south direction, see Fig. 6d-f. Additionally, the Witch/Fladen member boundary horizon underlying this appears to bow upwards to a maximum of 0.4 ms TWT. Directly below this zone, a distinct shadowing effect is visible, suggesting minimal penetration of the acoustic signal beyond this point. Below this the Fladen member appears acoustically unchanged.

Also visible in the seismic reflection data is highly reflective linear features connecting the underlying enhanced reflector with the seabed, see Fig. 6e and f. These chimney features appear to be only a few 10′s of centimetres in diameter, which is close to our minimum detection threshold. Immediately overlying them gas is clearly visible in the water column, escaping from a shallow depression in the seabed (~5 cm wide by 0.2 ms TWT deep). A 3D interpretation of this data set is given in Fig. 7.

5.1.4. Post release survey

By D + 16 (5 days after gas injection stopped) the seismic reflection data (Fig. 6g) appears to be similar to the pre-release data collected on D - 13 (Fig. 6a). The previously visible enhanced reflectors, bowing horizons, shadowing and chimneys are no longer present, leaving no acoustically visible evidence of the injection experiment.

5.2. Seismic evidence of CO_2 distribution in the subsurface

Seismic signatures related to increasing CO_2 saturation in the sediment include reflectivity enhancement and energy dissipation (Anderson and Hampton 1980). Energy loss is caused by bubble fractures present in the sediment, which resonate at certain frequencies and scatter the incident sound. We were able to compare the amplitude spectrum of the release site throughout the experimental period with that of a control site ~20 m east (see Fig. 8). The dominant frequency at the control site remained approximately constant (17,620 ± 100 Hz, at −30 dB) throughout the experiment. By contrast, at the release site the frequency (at −30 dB) decreased by ~2.5% from the pre- to the first syn-CO_2 release survey, this trend continuing to a total decrease of 3.7% (relative to the pre- release survey) by D + 6, before becoming constant thereafter up to the end of the CO_2 release. These changes could be related to a residual CO_2 fraction in the sediment or an alteration of the sediment properties or a combination of both.

Fig. 9 shows the root mean square (RMS) amplitude for a TWT time interval 1–3 ms beneath the seabed (~0.9–2.6 mbsf). As the presence of free gas greatly affects the impedance of sediment (Anderson and Hampton 1980) it is often clearly visible in RMS amplitude maps. On D + 3 when gas was being injected at 6 kg/day, the RMS amplitude at the release site (12.5 m radius around the injection point) was 0.033 ± 0.002 with no obvious hot spots. By D + 6 (at 29 kg/day), this average RMS value was unchanged across the release site, although a single "high amplitude" point of 0.040 (>1 m wide) had developed ~3 m north of the injection point. On D + 9, at the maximum flow rate (143 kg/day), a large high amplitude zone ~8 × 5 m wide of 0.045 had developed to the east of the central injection point. Meanwhile, the average RMS value across the release site remained constant. Spatially and geometrically, this zone is consistent with the enhanced bowing reflector seen in cross-section (Fig. 6e). The smaller high amplitude point seen on D + 6 was still visible, although it had migrated several meters north. The post-release survey on D + 16 (5 days after injection was stopped) shows that the high amplitude anomalies completely disappeared, and the whole site still had an RMS value of 0.033 ± 0.002, suggesting this is the natural undisturbed value for the sediment. It is thus logical to conclude the RMS changes are associated with the degree of CO_2 saturation within the sediments, with large high amplitude zones corresponding to gas pooling or chimney structures.

Fig. 10 shows the deformation of Horizon 2, the upper boundary of the Fladen member (i.e., top of the sandy layer seen in Fig. 3), using its observed depth on D + 3 as a baseline. D - 13 is not examined as the profile lines collected during this period were too sparse. Horizon 2 was selected as it is believed to lie directly above the potential gas pocket. Horizons beneath a gas pocket are more difficult to accurately position, especially on the decimetre scale, as the presence of gas alters the sound speed. Given the nature of uncertainty related to AUV positioning systems an error of ±0.25 ms TWT can be expected here. On D + 6 (29 kg/day injection rate) at the release site the horizon is 0.1 ms TWT closer to the seabed than on D + 3, well within positional error. However, on D + 9 Horizon 2 appears 0.40–0.50 ms TWT (0.3 ± 0.1 m) closer to the seabed than on D + 3 in a 10 × 7 m wide zone centred just east of the release point. This is a variation in depth too great to be a consequence

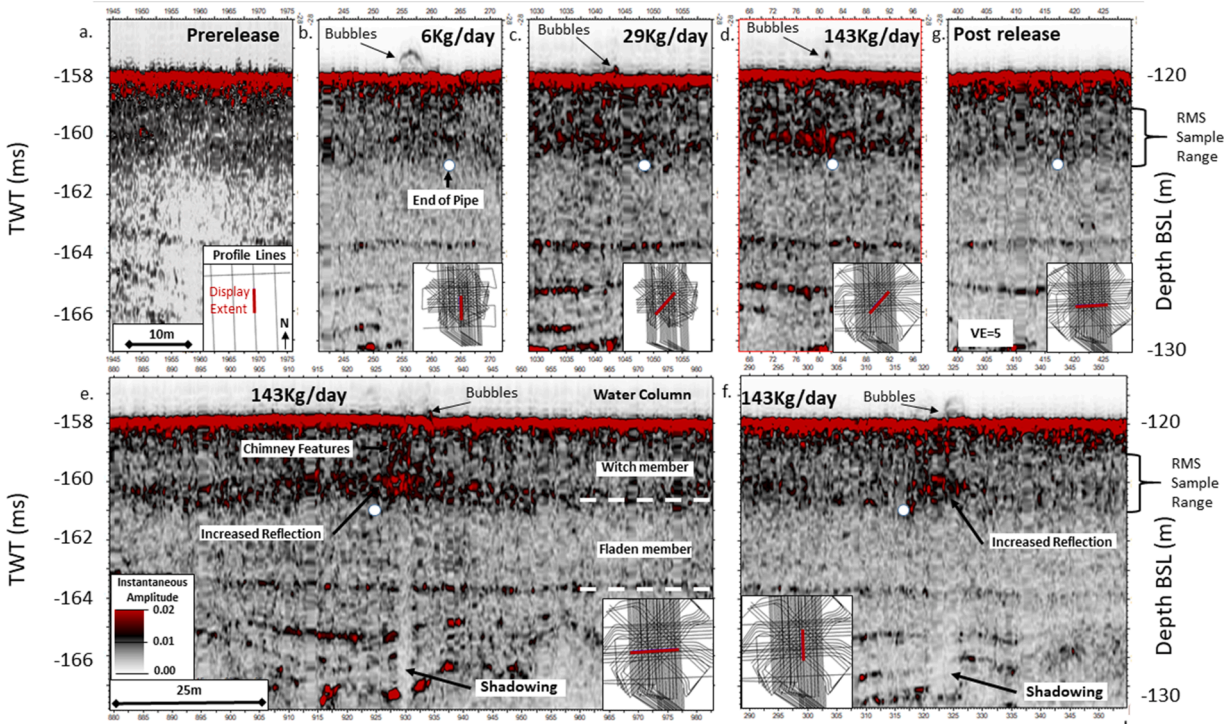

Fig. 6. Gavia 2D seismic reflection chirp data cross-section of the release site displaying the instantaneous amplitude. (a) D - 13 before injection (b) $D + 3$ at 6 kg/day injection, gas is visible in the water column but there is no evidence for gas in the underlying sediment; c) $D + 6$ at 29 kg/day injection rate there is no evidence of gas within the sediment (d-f) $D + 9$ at 143 kg/day injection, evidence of a gas pocket can be seen by the increased level of reflection from the base of the Witch member and the distinct shadow underneath. The column-like strong reflectors extending from the gas pocket to the seabed are likely gas chimneys, large scale fluid escape features. (g) $D + 16$ after injection was stopped all evidence of gas has disappeared and the image appears near identical to the pre-release profile shown in (a). Data is presented in two-way travel time (TWT) with the equivalent depth below sea level (BSL) provided.

of positional error. By $D + 16$, 5 days after gas injection was stopped, Horizon 2 appears 0.20–0.25 ms TWT closer to the seabed within the release site than on $D + 3$, again within positional error. Given the correlation with gas injection we suggest the apparent deformation of Horizon 2 is a direct consequence of the presence of gas.

This change could be related to (i) gas pooling in the sandy layer, resulting in sediment swelling and narrowing of the overlying Witch member; or (ii) due to the presence of gas in the overlying sediment increasing the seismic velocity via resonance. The latter option can be dismissed because the base of the horizon remains approximately constant (~2.32 ms TWT beneath the seabed) for the frequency range 15–20 kHz (i.e., frequency close to resonance). We are thus confident that the deformation of Horizon 2 is a real physical change caused by the pooling of gas within the upper sandy layer of the Fladen member.

5.3. CO_2 Volume estimation

To estimate the mass of injected CO_2 that can explain the uplift observed in our time-lapse seismic data for the base of the Witch member (Fig. 10), we assume it is caused by CO_2 injection in the pores and steady state conditions of CO_2 gas flow. Then, the change in sediment porosity over time is given by:

$$\frac{D\varphi(V_\varphi, V_s)}{Dt} = \frac{D}{Dt}\left(\frac{V_\varphi}{V_\varphi + V_s}\right) = \left(\frac{\frac{D}{Dt}V_\varphi(V_\varphi + V_s) - V_\varphi\frac{D}{Dt}V_\varphi}{(V_\varphi + V_s)^2}\right) = \frac{D\varepsilon_v}{Dt}(1-\varphi_0) \tag{4}$$

where φ_0 is the initial porosity before CO_2 injection, V_φ and V_s are the volume of pores and solid grains, respectively, and ε_v is the volumetric deformation which can be expressed as,

$$\varepsilon_v = \frac{\Delta V}{V_0} = \varepsilon_1 + \varepsilon_2 + \varepsilon_3 \tag{5}$$

where ΔV is the increment in sediment volume, V_0 is the initial sediment volume and $\varepsilon_1, \varepsilon_2, \varepsilon_3$ are the deformations in the three principal directions of strain. Assuming that the three principal directions of strain are orientated with the Cartesian coordinate system (x, y, z) and that deformations occur only in the vertical direction we obtain,

$$\varepsilon_v = \varepsilon_{zz} = \frac{\Delta H}{H_0} \tag{6}$$

where ΔH is the sediment uplift, and H_0 is the initial injection depth (the point at which gas enters the affected layer). Combining Eqs. (4) and 6 we can estimate the total change in porosity ($\Delta\varphi$) due to CO_2 injection as,

$$\Delta\varphi = \frac{\Delta H}{H_0}(1-\varphi_0) \tag{7}$$

To facilitate the calculation, we approximate the deformed volume to that of a cylinder with the height given by the uplift, and no CO_2 dissolution. Then, we can estimate the volume and mass of injected CO_2, as:

$$V_g = \Delta\varphi V_t = \Delta\varphi(\Delta H + H_0)\pi r^2 \tag{8}$$

$$M_g = V_g\rho_g \tag{9}$$

In Eqs. (8) and 9 V_g, M_g and ρ_g are the volume, mass, and density of CO_2 gas, respectively, V_t is the total volume of sediment, and r is the radius of the cylinder. To calculate the density of CO_2 we use the table for CO_2 thermophysical properties from the National Institute of Standards and Technology (*https://webbook.nist.gov/chemistry/fluid/*)

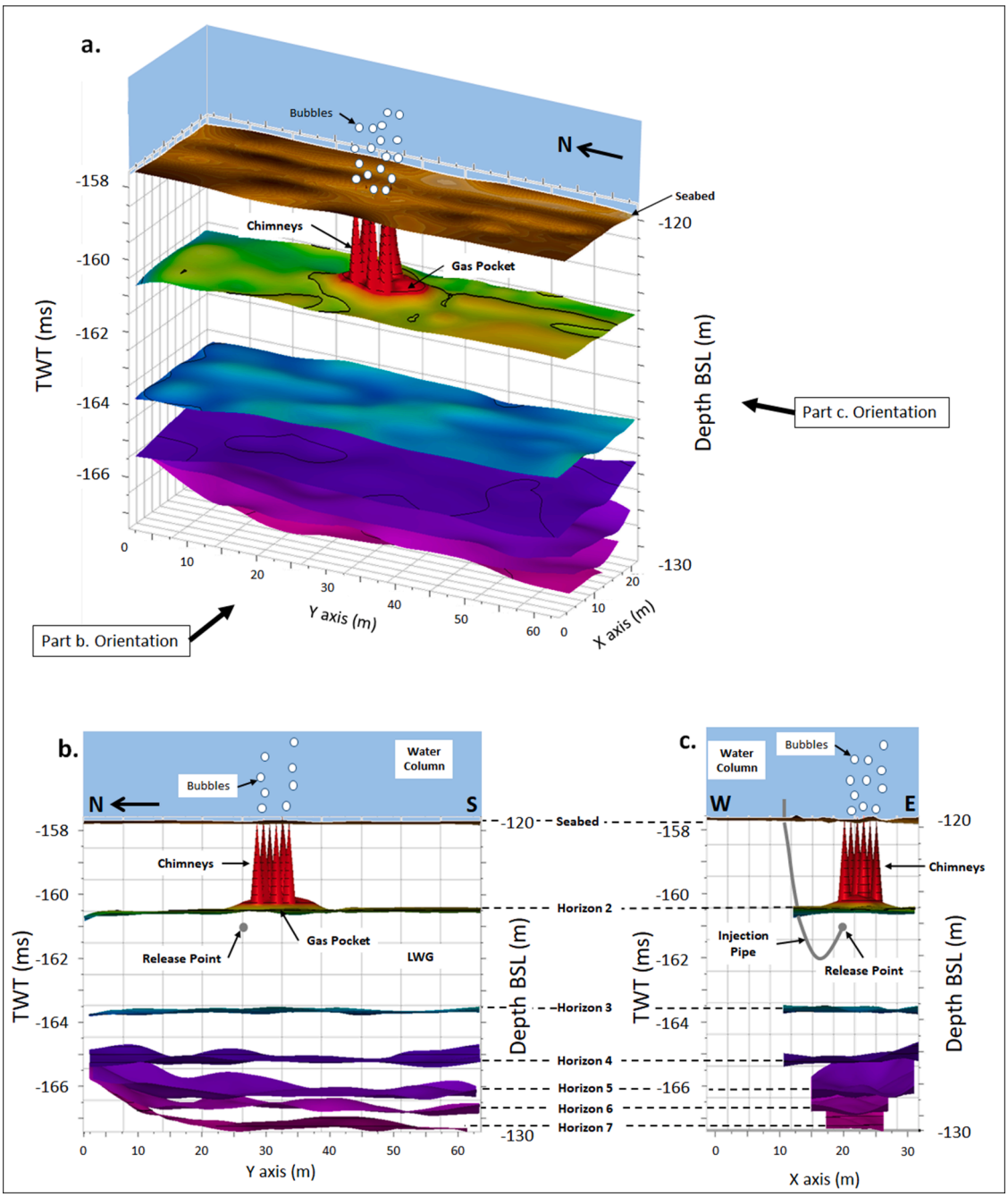

Fig. 7. 3D interpretation of seismic horizons directly beneath the release site at 143 kg/day injection rate with the resulting gas pocket and fluid escape features (chimneys) shown in red. a. Facing NE; b. facing East, release point indicated in grey, and c. facing north, release point and injection pipe indicated in grey. Data is presented in two-way travel time (TWT) with the equivalent depth below sea level (BSL) provided.

assuming the pressure and temperature conditions at half distance between the CO_2 injection depth and the seabed. Finally, the saturation of CO_2 gas (S_g) that explains the observed uplift can be estimated by,

$$S_g = \frac{V_g}{V_\varphi} = \frac{\Delta\varphi}{(\varphi_0 + \Delta\varphi)} \tag{10}$$

The elliptical dome observed in the dataset was 4.5 ± 0.5 m east-west, and 7.5 ± 0.5 m north-south, with a maximum height of 0.3 ± 0.1 m (Fig. 10b). A cylinder with the same sediment uplift and an equivalent volume has a radius of 2.4 ± 0.2 m. We consider an initial injection depth (the point at which gas enters the sandy layer) of 2.5 m, an initial porosity of 0.51 ± 0.05 (from logging; Fig. 3), a seabed temperature of 7 °C, a geothermal gradient of 0.03 °C/m. Using these values, we estimate that 91 ± 32 kg of CO_2 was retained in sediment on $D + 9$ (in gaseous form), which corresponds to a CO_2 saturation of 0.10 ± 0.03. The total volume of gas injected between raising the injection rate to 143 kg/day and the 3rd syn-release survey (when the pocket was visible) was 242 kg. We, therefore, suggest that 34 ± 12% of the injected gas remained within the sediment in the gaseous form during this period.

5.4. Hydrodynamic analysis

It is possible to calculate the permeability of the CO_2 pathways beneath the release site on $D + 9$ based on the observations of the gas pocket developing when the injection rate was at a maximum. If we assume one-dimensional poro-elastic expansion of the sediment, then

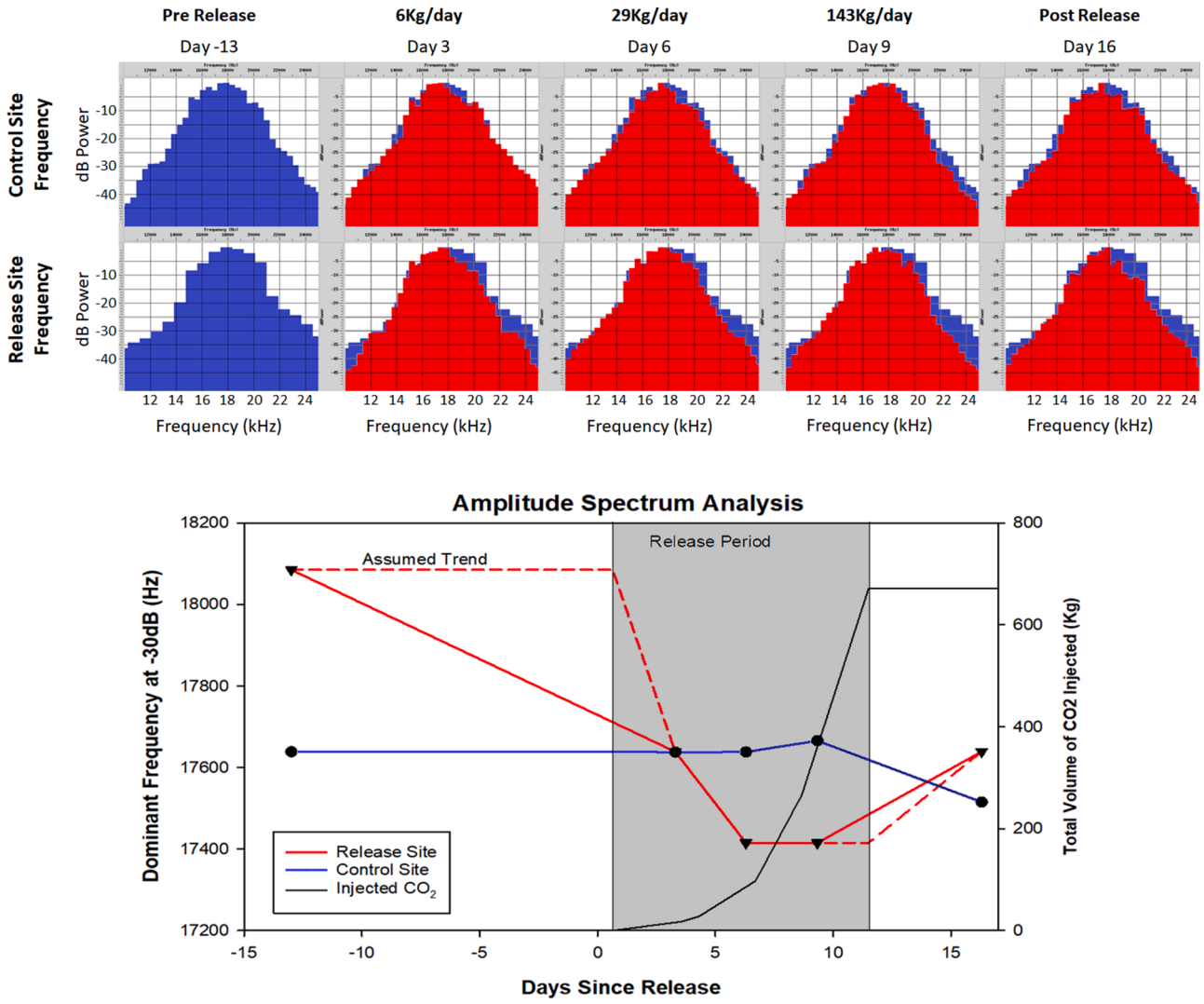

Fig. 8. Temporal and spatial variation of the seismic amplitude spectrum of 2D seismic reflection chirp data between 1 - 3 ms TWT below the seabed. (a) Amplitude spectrum of the seismic data at a control site and at the release site throughout the experiment (positions shown in Fig. 1c). Shown in blue is the pre-release spectrum for comparison. The release site shows a notable decrease in the presence of high frequency signals as soon as injection begins. (b) Graph of the dominant frequency at −30 dB at the control site (solid blue line) and the release site (solid red line). A decrease in dominant frequency is seen in the release site during the syn-release surveys, followed by an increase in the post-release survey. As we attribute the change in the release rate to the injection of gas, an interpreted trend (dashed red line) is also shown.

the amount of pore fluid overpressure (u) generating the inferred vertical uplift is given by (Wangen and Halvorsen, 2020).

$$u = \frac{\varepsilon_{zz}}{\alpha}\left(\frac{4}{3}G + K\right) \tag{11}$$

where G is the shear modulus of the sediment and α is the Biot's coefficient.

$$\alpha = 1 - \frac{K}{K_s} \tag{12}$$

In Eq. (12), K is the bulk modulus of the sediment at drained conditions, and K_s is the modulus of the solid grains. For the unconsolidated, soft sediments considered here, α can be assumed equal to 1.

We estimate our pore fluid overpressure for the maximum uplift of 0.3 m is ~0.35 ± 0.1 MPa, adopting representative values of the type of sediments within our depth of interest for K and G (~1 MPa). Our estimate is higher than that measured with a sensor at the end of the CO_2 injection pipe (~0.08 MPa). A better match can be found if the uplift was only ~0.1 m, which is not unrealistic if we imagine the sound speed is depressed by the presence of bubble fractures (Leighton and Robb 2008) causing us to slightly overestimate thickness. Using this value, we can also estimate the effective permeability of a CO_2 pathway connecting the injection depth with the seabed using Darcy's relationship:

$$k = \frac{Q \cdot \mu \cdot (\Delta H + H_0)}{k_{rg} \cdot A \cdot (u - f \cdot u)} \tag{13}$$

where Q is the volumetric CO_2 bubble flow measured at the seabed, μ is the dynamic viscosity of CO_2, k_{rg} is the relative permeability of CO_2 gas, A is the area of the CO_2 pathway (i.e., the area perpendicular to the measured gas flow), and f is a dimensionless parameter between 0 and 1 controlling the fraction of pore fluid overpressure just below the seabed. Here, as observed in gas migration laboratory experiments in unconsolidated, soft, fine-grained, cohesive sediments (e.g., Algar et al., 2011), we can assume that the pathways are fully saturated in CO_2 gas (dry pathways), and so k_{rg} is equal to 1. Based on our discussion above, we note this is a simplification as in reality the gas bubble fracture walls are wet.

If we consider the values used and calculated above for the estima-

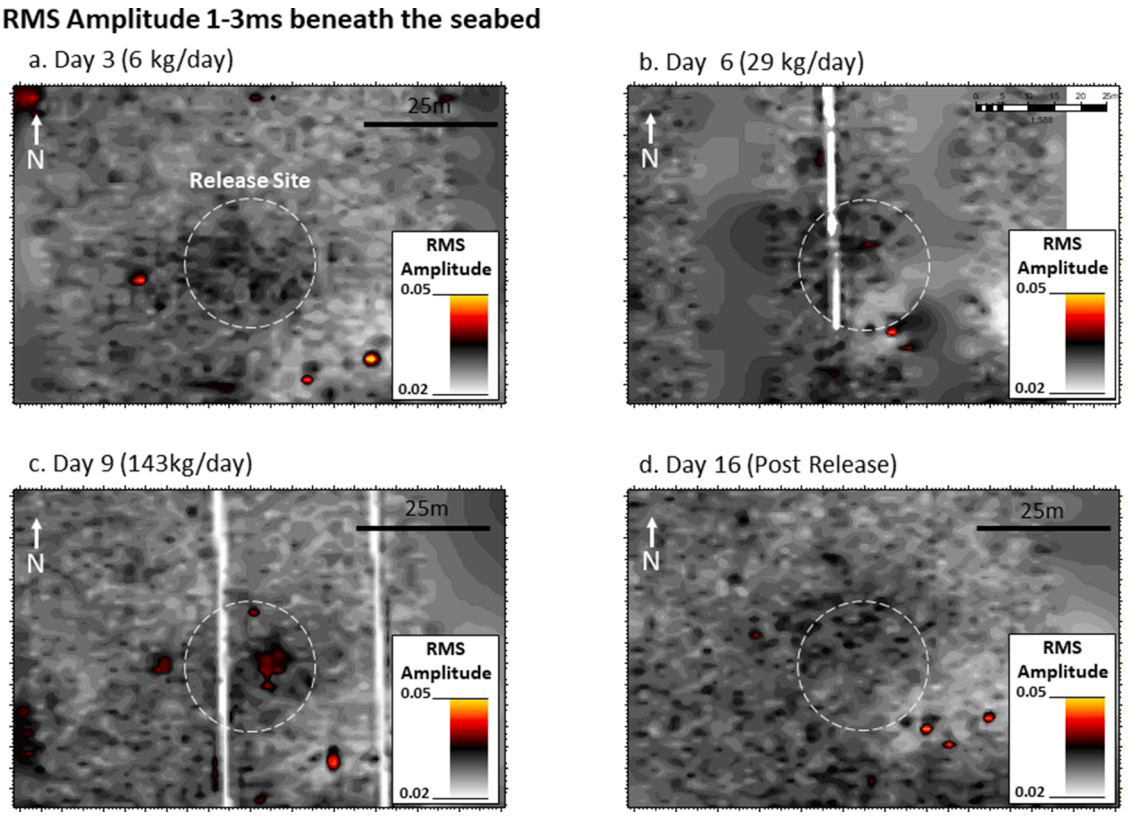

Fig. 9. Chronological maps of RMS amplitude (1 – 3 ms TWT beneath the seabed) over the experimental site with the release point located in the centre of the white circle. a) $D + 3$ at 6 kg/day b) $D + 6$ at 29 kg/day c) $D + 9$ at 143 kg/day d) $D + 16$ post release. Note the appearance of a high amplitude zone at 143 kg/day that then disappears post injection. Linear white zones during $D + 6$ and $D + 9$ are due to errors in data collection resulting in unusable profile lines. Anomalies outside the release area are deemed to be either noise or the result of reflections from experimental landers on the seabed.

tion of the CO_2 mass within the uplift area, a Q of 0.05 m^3/s, a CO_2 pathway area A of $20m^2$, an f of 0.5, and a CO_2 viscosity with pressure and temperature conditions at half distance between the CO_2 injection depth and the seabed of 1.48×10^{-5} Pa s (CO_2 thermophysical properties from the National Institute of Standards and Technology; https://webbook.nist.gov/chemistry/fluid/), the effective permeability of the CO_2 pathway is $\sim 2 \times 10^{-14}$ m^2. Falcon-Suarez et al (this issue) used core analysis to estimate the effective permeability of water in the Witch Ground (collective term for Witch and Fladen members), away from the injection site, to be 2×10^{-17} m^2, 1000 times lower than our estimate, emphasizing the effect chimney structures have on the rate of gas flow through the near-surface.

5.5. Crack size calculations

Using measured physical sediment properties in conjunction with Eq. (2), it is possible to calculate the critical size of bubble fractures/cracks a_r undergoing stable fracture propagation at different depths in the near subsurface (Fig. 11). There is broad agreement between sediment type and critical crack size due to the relationship between crack size and solid grain density, water density, porosity, and the sediment fracture toughness. With reference to the observed seismic horizons, low values of crack length (2.6 mm) occur from the seabed to Horizon 1, across which there is an increase to ~ 3.0 mm. These higher values continue down to Horizon 2, where the increase in sand content causes a decrease in crack length to 2.7 mm.

These variations in crack size have important implications for the propagation of a bubble fracture moving upwards through the sediment. Given the coarse nature of sediment immediately below Horizon 2 gas likely migrates via capillary invasion before transitioning to stable fracture propagation above the Horizon; the size of the fracture changing with sediment type. If a fracture exceeds the critical crack length, it will instead begin to migrate via dynamic fracture propagation (Katsman 2019). The size of a rising bubble fracture does not decrease instantaneously, thus the large and rapid decrease in critical crack size across Horizon 1 will likely result in a transition into dynamic propagation which may control gas migration to the seabed. This may cause an increase in free gas permeability in the sediment above that measured in the pre-release sediment cores.

6. Discussion

6.1. Migration of CO_2 in sub-seabed sediments at the release site

Based on the temporal and spatial development of the acoustic anomalies seen during the CO_2 release experiment along with visual seabed seep observations we propose a four-stage model for the evolution of gas migration pathways in the sub-surface (Fig. 12):

Stage 1 – Proto-migration: the initial migration of gas immediately following the start of CO_2 injection where individual bubbles make their own way to the surface via capillary invasion, stable and dynamic fracture propagation with no preferred pathways. Many routes will be highly inefficient, and some gas will fail to reach the seabed.
Stage 2 – Immature migration: the migration of gas occurs along preferred pathways via capillary invasion, stable and dynamic fracture propagation forming small temporary seeps on the seabed. Dynamic fracture propagation becomes more dominant as time goes on.
Stage 3 – Mature migration: the migration of gas has been optimised and occurs via open conduits or chimneys, connecting a gas reservoir

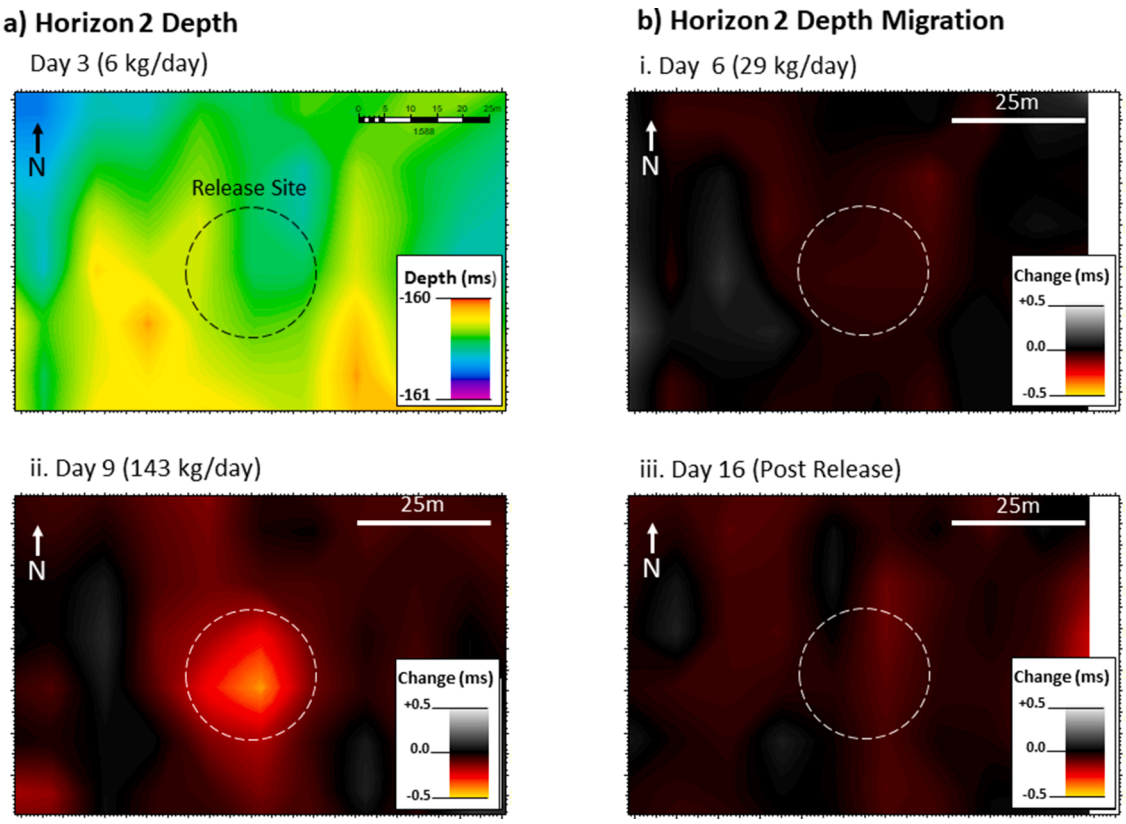

Fig. 10. Map of the release site with the release point located in the centre of the white circle showing a) the depth of Horizon 2 on $D + 3$ in TWT, b) the change in the depth of Horizon 2 relative to its position on $D + 3$ (i) on $D + 6$ at 29 kg/day injection rate, (ii) on $D + 9$ at 143 kg/day injection rate and (iii) on $D + 16$, 5 days after injection had stopped.

to the surface (or a secondary reservoir) forming moderate to large seeps on the seabed.

Stage 4 – Closure: migration pathways have closed completely following the end of the gas injection. The system reverts to its pre migration state.

These stages are universally applicable to any near-surface seep site as general descriptors of the gas migration pathways. However, the exact length of time spent within each stage and transition between stages will vary with stratigraphy, grainsize and injection rates etc. Indeed, many seeps likely do not reach the mature stage and simply skip to the final stage from stage 2 or even stage 1 in the case of sporadic ebullition sites.

The following is a hypothesis for the dynamic gas processes within the sediment during each stage consistent with observations made in this paper.

Stage 1 - Proto Migration

The Proto-migration stage is the initial chaotic migration of gas with no preferential pathways established immediately following release (within a few hours) and cannot be imaged by acoustic methods.

While we have no direct imaging of gas migration during this phase, based on existing gas propagation theory and gravity core data we speculate the following. During the release experiment CO_2 was injected directly into the Fladen member at a depth of ~3 mbsf. The pressure from the end of the injection pipe likely generated a small fracture network into which the gas escaped. From here the gas would have migrated upwards into an overlying sand layer, ~0.5 m thick. Within the sandy layer gas would have begun migrating via capillary invasion as the larger grain size would have made fracture propagation difficult. After migrating through this layer, the finer-grained sediments within the Witch member favoured migration via stable fracture propagation, the steady rise of single bubble fractures. The gas would rise through the sediment as an upward propagating crack, sealing behind itself in order to maintain a constant pressure. Eventually, at ~1.4 mbsf depth the bubble fractures cross a grain size boundary (Horizon 1) in which the sediment is significantly weaker, and a much smaller crack size is required for stable fracture propagation (Fig. 11). As the bubble fractures rising to this depth are much larger than this critical fracture size, they begin to migrate via dynamic fracture propagation. The bubble crack grows rapidly upward until reaching the seabed, at which point the gas is released into the water column and the fracture closes. This interpretation is based on seabed observations and the application of LEFM to gravity core analysis. The first phase lasted less than a few hours as the first seeps were visible on the seabed within 12 h, indicating the appearance of preferred pathways.

Stage 2 – Immature Migration

The immature migration stage is an early step in the evolution of the system, with the establishment of preferred fluid-flow routes. The passage of a bubble fractures weakens the sediment making the subsequent passage of gas more likely, thus creating a positive feedback loop that slowly builds stable fracture propagation pathways over time. These pathways are small (perhaps <1 cm in diameter) and easily destroyed by overlying pressure fluctuations i.e., internal waves in the water column, which compress sediment within the pathway (strengthening it) causing the bubble fractures to find an alternative route. It is at this stage that seeps are first seen on the seabed, though they are generally temporary in nature, becoming extinct as underlying pathways close. This is the stage most subject to change as the system slowly matures overtime, pathways will become less and less mobile before eventually becoming fixed in place and expanding. Acoustically this stage transition may be

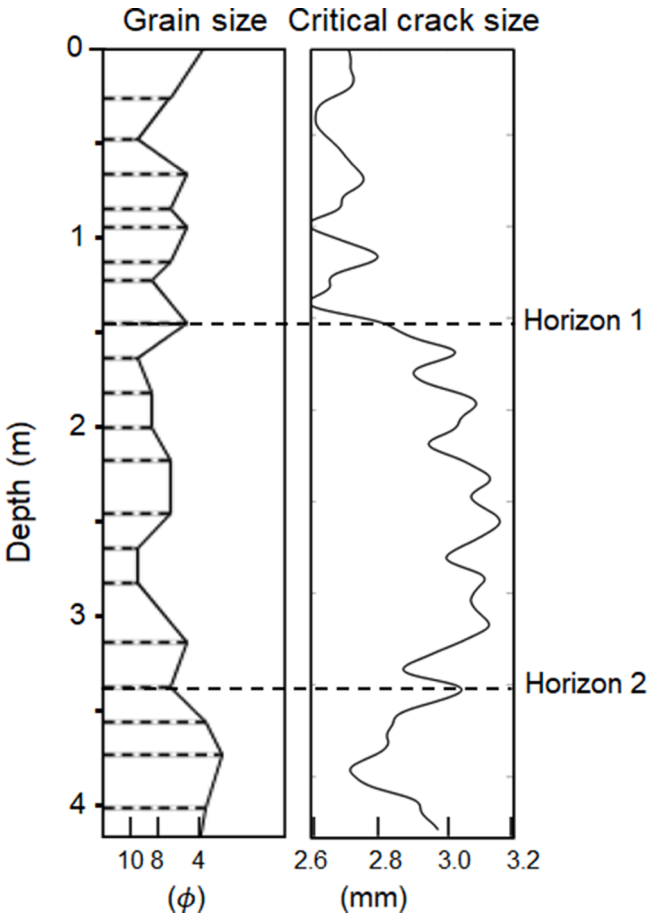

Fig. 11. The minimum critical size (crack length) for a bubble fracture to rise through the sediment of a specific grain size. (Left) grain size variations down core GC06; (Right) Crack length calculated using Eq. (2). Significant changes in crack length are observed at Horizon 1 and 2.

visible in the water column, but it is very hard to identify in the subsurface, except via comparison with the bulk acoustic properties of the sediment pre-release.

Day 3 (injection rate 6 kg/day) was our first acoustic observation of the system at this stage during the release experiment. Seeps are present and are highly mobile, regularly appearing and disappearing on the seabed as seen by ROV observations at the release site (Flohr et al., 2021). A lack of distinct acoustic anomalies in the subsurface suggests no gas was retained in the sediment as shown by clear evidence of gas release in the water column. However, the passage of gas through the sediment caused attenuation of seismic energy, decreasing the dominant frequency. That a quantifiable change can be detected at such an early stage of release, at such a low CO_2 injection rate, suggests spectral analysis of acoustic data could be a useful tool for detection. By day 6 of the release experiment (injection rate 29 kg/day) gas is continuing to flow directly from the release pipe to the surface. Fluid migration pathways are still mainly in the form of weakened stable propagation channels that are small and mobile, though the higher flow rate has resulted in a greater number of pathways (and thus seeps). The continued lack of distinct acoustic anomalies in the subsurface suggests that no gas is retained in the sediment. The level of attenuation has increased to a maximum at this point, with the dominant frequency plateauing. It is impossible to tell whether this maximum was reached due to the increased flow rate or due to the total volume of gas that had passed through the sediment by this stage.

By day 7 of the release experiment (injection rate of 86 kg/day), we hypothesise that the flow rate out of the sandy layer at the top of the Fladen member had been exceeded by the inflow rate of gas from the injection pipe fracture network, resulting in the pooling of gas within the layer. This causes the unit to slowly expand in a localised area around the release site. While no seismic reflection survey was carried out during this period, later surveys do show clear evidence of pooling and ROV surveys on $D + 7$ showed that no new seeps were formed as a result of increasing the injection rate and the nature of the existing seeps had not significantly changed (Flohr et al., 2021), suggesting the amount of gaseous CO_2 escaping into the water column had remained unchanged despite the rate.

Stage 3 – Mature Migration

The mature stage of gas migration is the point at which gas flow through the near-surface has been optimised. Migration is no longer via stable or dynamic fracture propagation but through stable open conduits, named here chimney structures, which allow the gas to pass unrestricted from a reservoir (primary or secondary) to the surface. This stage of gas migration is the most seismically visible as chimney structures leave distinct acoustic anomalies. This stage is also of the greatest interest to environmental studies as the high flow rate of gas through the sediment reduces the residence time of gas in the near-surface and thus increases the volume of gas released into the water column.

We propose that the expansion of the extent of the sub-surface where gas migration occurs by dynamic fracture propagation (and a corresponding decrease in the zone of stable fracture propagation) is fundamental to the formation of mature gas migration systems. The original position of the stable/dynamic propagation boundary is dictated by local pressure conditions and sediment properties (i.e., a sudden decrease in grain size over the boundary causes a decrease in critical crack size triggering dynamic fracture propagation). Within the stable propagation zone, the continuous passage of gas weakens the sediment allowing for an increased flow rate of gas and eventually, the gas bubble fractures begin to propagate into each other causing them to exceed the critical crack length and transition to dynamic fracture propagation. While such collisions could occur at any point within the stable propagation zone the presence of (momentarily) lingering dynamic fractures across the boundary makes the chances of such events significantly more likely just below the boundary. Hence slowly over time the dynamic fracture propagation zone advances into the stable propagation zone, provided the level of gas flux is sufficient and continuous. This will occur until the dynamic propagation zone covers the full length of the near-surface, from some form of gas reservoir to the seabed. Connecting to a gas reservoir greatly increases the volume of gas supplied to dynamic fractures such that the internal pressure of the gas flowing through the crack is sufficient to keep the crack open for an extended period of time. This allows for the formation of open conduits, chimney structures, connecting gas reservoirs to the seabed. At this point, the gas flow can be thought of as reaching a “mature state” whereby the gas flow is constant, and the pathways are essentially rooted in place. Across a greater depth of unconsolidated sediment (100 s of meters) it is easy to imagine this process repeating itself multiple times between a series of small gas pockets until large scale chimney structures are formed as seen in Landrø et al. (2019).

By day 9 of the release experiment (injection rate of 143 kg/day) gas has pooled sufficiently in the sandy base of the Witch member to form an elliptical dome-shaped gas pocket ~8 × 5 m wide with a maximum height of ~0.3 m. The gas pocket is evident by the bowing seismic horizon, enhanced reflectors, shadowing, high-frequency attenuation and increased RMS amplitude within this layer. The gas pocket contains 91 ± 32 kg of CO_2 (see Section 5.3) which is equal to approximately half the total volume of gas injected since upping the flow rate to 86 kg/day. Fluid pathways are now open channels within the sediment allowing gas/bubble fractures to rise unrestricted. These pathways are larger and more permanent gas conduits (the overlying seeps being far less mobile) visible in the seismic data as chimneys, connecting the gas pocket (now

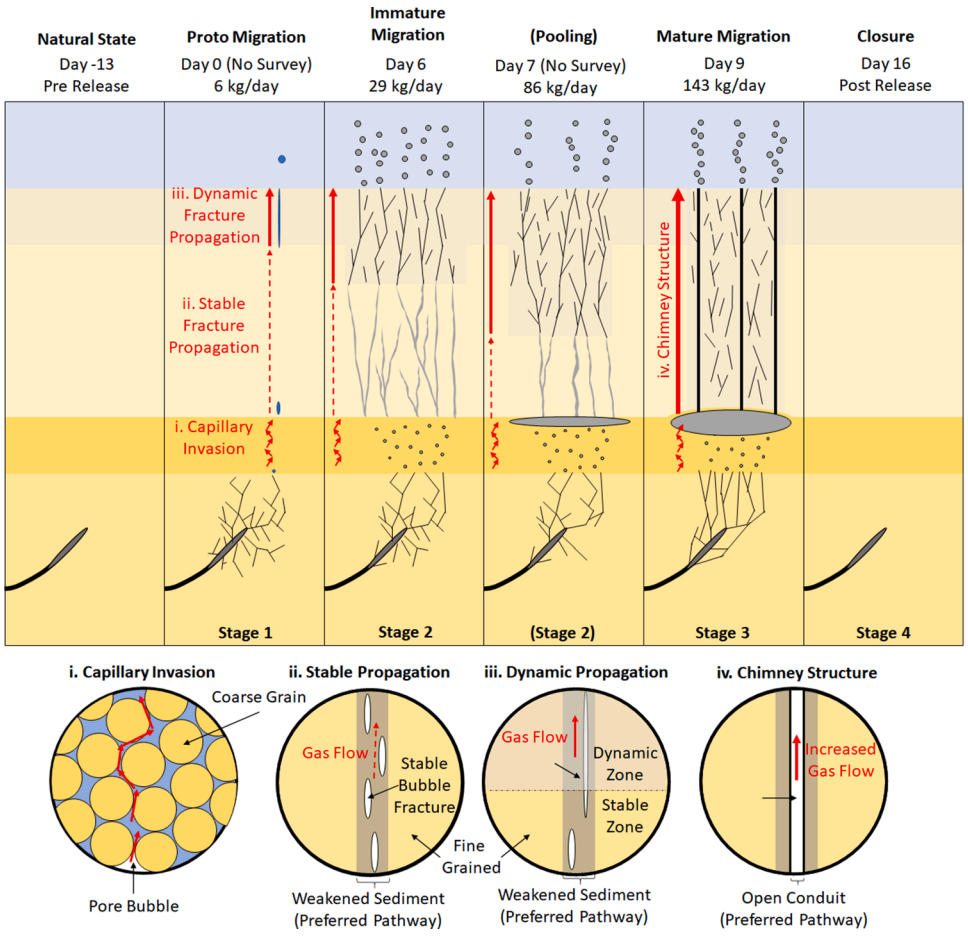

Fig. 12. Schematic interpretation of gas migration during the release experiment and stages in the evolution of gas migration pathways. **Day 0)** the "proto migration" stage that occurs immediately after the start of CO_2 injection, where individual gas bubble fractures make their way to the surface with no preferred pathways. **Day 6)** the "immature migration" phase of the experiment where a number of temporary pathways have developed along which most bubble fractures travel. The depth below the seabed at which dynamic fracture propagation occurs increases over time. **Day 7)** the rate at which gas was being injected into the sediment (86 kg/day) exceeded the rate at which gas could migrate through the coarse sand layer and pooling of gas begins. **Day 9)** during the "mature migration" phase the dynamic fracture propagation zone extends to the gas reservoir allowing open conduits to form between the reservoir and the overlying water column. **Day 16)** the system has experienced the "closure" phase following the end of the CO_2 injection and the sediment has almost reverted to its original state (**Day −13**).

essentially acting as a secondary reservoir) to the surface. The formation of these open conduits has significantly increased the effective CO_2 permeability of the near-surface to 2×10^{-14} m^2. Given the nature of this experiment we cannot say confidently whether these larger open conduits formed as a consequence of the increased injection rate or the length of time the pathways had been active, most probably both contributed. The dynamic propagation zone most likely slowly progressed downwards from an original depth of 1.4 mbsf throughout the "immature migration" stage, the rate of this progression increasing with the injection rate. The dynamic propagation zone reached the newly formed gas reservoir in the sand layer at some point between $D + 6$ and $D + 9$ (when chimney structures were first seen).

Fig. 13 is our interpretation of the expansion of the dynamic fracture propagation zone over time during the release experiment. Initially, at lower flux rates the change was minimal, but as the injection rate increased so too did the rate of expansion.

Stage 4 – Closure

The closure stage is the final phase of the gas migration lifecycle. Once gas is no longer being injected into the system the inflow of gas through the open pathways stops. Without the outward pressure of the flowing gas, the channels close. Any remaining free gas migrates via stable/dynamic fracture propagation or dissolved into the sediment pore water.

CO_2 injection was stopped on day 11 of the experiment and bubble seeps were no longer observed within an hour. This suggests that the gas pocket had already deflated following the increased flow rate through the open fluid conduits. By day 16 (5 days after the gas release stopped) the subsurface was completely devoid of acoustic anomalies and

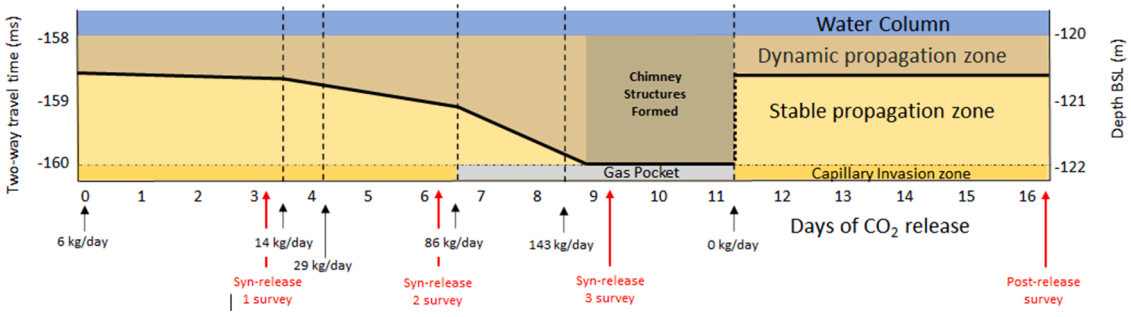

Fig. 13. Temporal changes in the dominant form of gas migration during the CO_2 release experiment. The depth of sediments where dynamic fracture propagation dominates expands with time and eventually connects the gas pocket with the seabed.

appeared identical to the pre-release survey. It is likely that the chimney structures closed almost instantly once the passage of gas stopped, leaving only the surface craters which would be slowly infilled with sediment.

These stages of the evolution of gas migration pathways can also be applied to the QICS release experiment. In the QICS experiment, CO_2 gas was injected 11 m below the seabed of a shallow bay in western Scotland, into fine-grained sediment overlaid by coarser sandy sediment (Cevatoglu et al., 2015; Taylor et al., 2015). Proto-migration occurred with dynamic fracture propagation within the muddy sediment immediately surrounding the injection point up to the base of the sandy layer. The weight of the sediment initially prevented fracture propagation, leading to the pooling of gas, though some individual bubbles were able to escape to the surface (Cevatoglu et al., 2015). During the immature migration stage gas migration through the upper sandy layer slowly transitioned from primarily via capillary invasion to primarily via fracture propagation, with a number of seeps forming on the seabed. Once the mature migration stage was reached dynamic propagation pathways extended all the way from the injection point through the overlying sand and to the seabed, forming open conduits over the entire length of the near-surface (Cevatoglu et al., 2015). We note that in QICS, unlike in STEMM-CCS, the dynamic fracture propagation boundary migrated upwards (not downwards) highlighting that what is important is the extension of the dynamic fracture propagation zone within the sub-surface rather than its depth. Finally, in the closure stage following the end of the gas release experiment the flow of gas into the water column stopped almost instantly and subsequent seismic surveys found no evidence of lasting alteration to the subsurface (Cevatoglu et al., 2015).

7. Conclusions

We have used pseudo-3D time-lapse high-resolution chirp seismic reflection imaging of a controlled CO_2 release experiment to map the evolution of gas migration pathways in near-surface sediments. The seismic data, alongside gravity core and hydrodynamic analysis as well as volume estimation modelling, reveals a transition in the primary method of gas migration, from stable fracture propagation to dynamic fracture propagation, and finally the formation of semi-permanent open pathways (chimney structures). These observations have been used to interpret four distinct stages in the evolution of a gas migration system.

During the first stage lasting only a few hours (CO_2 injection rate = 6 kg/day) injected gas made its way to the surface as individual bubble fractures, escaping as discrete ebullition events into the water column. Stage 2 (D+~0.5 to D + 8, CO_2 injection rate = 6 - 29 kg/day) began as small unstable gas migration pathways were formed that focused the flow of gas to a number of seeps on the seabed. These gas conduits were easily destroyed (presumably by changing pressure conditions) and regularly reformed in new positions, leading to the continuous termination and creations of new seeps. Once the injection rate of the gas began to exceed the flow rate of the gas through the sediment gas started to pool and an ellipsoid shaped gas pocket became visible in the subsurface. We estimate that 242 kg of gas were trapped in the gas pocket, which is consistent with physical estimates that indicated that ~50% of the injected CO_2 flowed directly into the water column (Flohr et al., 2021).

The major gas migration phase, Stage 3, (D + 8 to D + 11 CO_2 injection rate = 143 kg/day) began when open conduits, chimneys, formed connecting the gas pocket to the seabed maximising the flow of gas to the near-surface and sharply increasing the effective permeability of the sediments by three orders of magnitude to 2×10^{-14} m^2. The seismic chimneys were clear in the seismic reflection data. The final stage 4 (D + 11, CO_2 injection rate = 0 kg/day) began when CO_2 injection had stopped. The remaining gas in the sediment escaped into the water column along the chimney features, after which following a loss of internal pressure the conduits closed. Acoustically the system reverted to its pre-release state (within 5 days), except for the subtly increased levels of attenuation, which recovers at a much slower rate, suggesting such observations could be used to detect episodic events.

Author statement

B.R & J.B conceived the survey; B.R & M.F processed the seismic data; M.T and A.L analysed the gravity core. All authors contributed to the writing of this manuscript.

Declaration of Competing Interest

The authors declare that they have no known competing financial interests or personal relationships that could have appeared to influence the work reported in this paper.

Acknowledgements

The STEMM-CCS project has received funding from the European Union's Horizon 2020 research and innovation programme under grant agreement No. 654462. We would like to acknowledge the hard work, enthusiasm, and professionalism of the crews and operators of the RRS *James Cook*, the RV *Poseidon*, the ROV Isis and the AUV Gavia who made the experiment possible. In addition, the authors would like to thank the following who enabled the project and experiment to take place: the staff at Air Liquide UK Ltd., Bronkhorst UK Ltd., Cellula Robotics Ltd., City Gas EOOD, Corsyde International GmbH, DG Pipe Services Ltd., J & J Engineering (Southampton) Ltd., Protea Ltd., and Sourceways Ltd. The British Ocean Sediment Core Research Facility (BOSCORF) is thanked for their expertise and facilities. We are also grateful to Schlumberger Ltd for the donation of Petrel software to the University of Southampton.

Supplementary materials

Supplementary material associated with this article can be found, in the online version, at doi:10.1016/j.ijggc.2021.103363.

References

Algar, C.K., Boudreau, B.P., Barry, M.A., 2011. Initial rise of bubbles in cohesive sediments by a process of viscoelastic fracture. J. Geophys. Res. 116, B04207. https://doi.org/10.1029/2010JB008133.

Anderson, A.L., Abegg, F., Hawkins, J.A., Duncan, M.E., Lyons, A.P., 1998. Bubble populations and acoustic interaction with the gassy floor of Eckernforde Bay. Cont. Shelf Res. 18 (14–15), 1807–1838.

Anderson, A.L., Hampton, L.D., 1980a. Acoustics of gas-bearing sediments I. Background. J. Acoust. Soc. Am. 67 (6), 1865–1889.

Barry, M.A., Johnson, B.D., Boudreau, B.P., 2012. A new instrument for high-resolution in situ assessment of Young's modulus in shallow cohesive sediments. Geo-Marine Lett. 32, 349–357. https://doi.org/10.1007/s00367-012-0277-z.

Blackford, J., Artioli, Y., Clark, J., de Mora, L., 2017. Monitoring of offshore geological carbon storage integrity: implications of natural variability in the marine system and the assessment of anomaly detection criteria. Int. J. Greenh. Gas Control 64, 99–112. https://doi.org/10.1016/j.ijggc.2017.06.020.

Blackford, J., Stahl, H., Bull, J.M., Bergès, B.J.P., Cevatoglu, M., Lichtschlag, A., Connelly, D., James, R.H., Kita, J., Long, D., Naylor, M., Shitashima, K., Smith, D., Taylor, P., Wright, I., Akhurst, M., Chen, B., Gernon, T.M., Hauton, C., Hayashi, M., Kaieda, H., Leighton, T.G., Sato, T., Sayer, M.D.J., Suzumura, M., Tait, K., Vardy, M. E., White, P.R., Widdicombe, S., 2014. Detection and impacts of leakage from sub-seafloor deep geological carbon dioxide storage. Nat. Clim. Chang. 4, 1011–1016. https://doi.org/10.1038/nclimate2381.

Blair, T.C., McPherson, J.G., 1999. Grain-size and textural classification of coarse sedimentary particles. J. Sediment. Res. 69, 6–19. https://doi.org/10.2110/jsr.69.6.

Böttner, C., Berndt, C., Reinardy, B.T.I., Geersen, J., Karstens, J., Bull, J.M., Callow, B.J., Lichtschlag, A., Schmidt, M., Elger, J., Schramm, B., Haeckel, M., 2019. Pockmarks in the Witch Ground Basin, Central North Sea. Geochem., Geophys. Geosyst. 20, 1698–1719. https://doi.org/10.1029/2018GC008068.

Boudreau, B.P., 2012. The physics of bubbles in surficial, soft, cohesive sediments. Mar. Pet. Geol. 38, 1–18. https://doi.org/10.1016/j.marpetgeo.2012.07.002.

Boudreau, B.P., Algar, C., Johnson, B.D., Croudace, I., Reed, A., Furukawa, Y., Dorgan, K. M., Jumars, P.A., Grader, A.S., Gardiner, B.S., 2005. Bubble growth and rise in soft sediments. Geology 33, 517. https://doi.org/10.1130/G21259.1.

Cevatoglu, M., Bull, J.M., Vardy, M.E., Gernon, T.M., Wright, I.C., Long, D., 2015. Gas migration pathways, controlling mechanisms and changes in sediment acoustic

properties observed in a controlled sub-seabed CO 2 release experiment. Int. J. Greenh. Gas Control 38, 26–43. https://doi.org/10.1016/j.ijggc.2015.03.005.
Dean, M., Blackford, J., Connelly, D., Hines, R., 2020. Insights and guidance for offshore CO2 storage monitoring based on the QICS, ETI MMV, and STEMM-CCS projects. Int. J. Greenh. Gas Control.
Dean, M., Tucker, O., 2017. A risk-based framework for Measurement, Monitoring and Verification (MMV) of the Goldeneye storage complex for the Peterhead CCS project, UK. Int. J. Greenh. Gas Control. 61, 1–15. https://doi.org/10.1016/j.ijggc.2017.03.014.
Dlugokencky, E.J., Nisbet, E.G., Fisher, R., Lowry, D., 2011. Global atmospheric methane: budget, changes and dangers. Philos. Trans. R. Soc. A Math. Phys. Eng. Sci. 369, 2058–2072. https://doi.org/10.1098/rsta.2010.0341.
Faggetter, M.J., Vardy, M.E., Dix, J.K., Bull, J.M., Henstock, T.J., 2020. Time-lapse imaging using 3D ultra-high-frequency marine seismic reflection data. Geophysics 85, P13–P25. https://doi.org/10.1190/geo2019-0258.1.
Falcon-Suarez I.H., et al., "CO2 flow-through experiment using pockmark seabed samples, with of geophysical and hydro-mechanical, and chemical monitoring" [working title] *International Journal of Greenhouse Gas Control – STEMMCCS special issue (This issue)*.
Friedlingstein, P., Jones, M.W., O'Sullivan, M., Andrew, R.M., Hauck, J., Peters, G.P., Peters, W., Pongratz, J., Sitch, S., Le Quéré, C., Bakker, D.C.E., Canadell, J.G., Ciais, P., Jackson, R.B., Anthoni, P., Barbero, L., Bastos, A., Bastrikov, V., Becke, S., 2019. Global Carbon Budget 2019 ETH Library. Earth Syst. Sci. Data. https://doi.org/10.3929/ethz-b-000385668.
Flohr, A., Schaap, A., Achterberg, E.P., Alendal, G., Arundell, M., Berndt, C., Blackford, J., Böttner, C., Borisov, S.M., Brown, R., Bull, J.M., Carter, L., Chen, B., Dale, A.W., de Beer, D., Dean, M., Deusner, C., Dewar, M., Durden, J.M., Elsen, S., Esposito, M., Faggetter, M., Fischer, J.P., Gana, A., Gros, J., Haeckel, M., Hanz, R., Holtappels, M., Hosking, B., Huvenne, V.A.I., James, R.H., Koopmans, D., Kossel, E., Leighton, T.G., Li, J., Lichtschlag, A., Linke, P., Loucaides, S., Martínez-Cabanas, M., Matter, J.M., Mesher, T., Monk, S., Mowlem, M., Oleynik, A., Papadimitriou, S., Paxton, D., Pearce, C.R., Peel, K., Roche, B., Ruhl, H.A., Saleem, U., Sands, C., Saw, K., Schmidt, M., Sommer, S., Strong, J.A., Triest, J., Ungerböck, B., Walk, J., White, P., Widdicombe, S., Wilson, R.E., Wright, H., Wyatt, J., Connelly, D., 2021. Towards improved monitoring of offshore carbon storage: a real-world field experiment detecting a controlled sub-seafloor CO2 release. Int. J. Greenh. Gas Control 106, 103237. https://doi.org/10.1016/j.ijggc.2020.103237.
Furre, A.-K., Eiken, O., Alnes, H., Vevatne, J.N., Kiær, A.F., 2017. 20 Years of Monitoring CO2-injection at Sleipner. Energy Procedia 114, 3916–3926. https://doi.org/10.1016/j.egypro.2017.03.1523.
Hansen, O., Gilding, D., Nazarian, B., Osdal, B., Ringrose, P., Kristoffersen, J.-.B., Eiken, O., Hansen, H., 2013. Snøhvit: the History of Injecting and Storing 1 Mt CO2 in the Fluvial Tubåen Fm. Energy Procedia 37, 3565–3573. https://doi.org/10.1016/j.egypro.2013.06.249.
IEAGHG, 2013. Information Sheets for CCS. https://ieaghg.org/docs/General_Docs/Reports/2013-16_Information_Sheets_for_CCS_All_sheets.pdf.
Irwin, G.R., 1957. Analysis of Stresses and Strains Near the End of a Crack Traversing a Plate. J. Appl. Mech. 24, 361–364.
Jain, A.K., Juanes, R., 2009. Preferential Mode of gas invasion in sediments: grain-scale mechanistic model of coupled multiphase fluid flow and sediment mechanics. J. Geophys. Res. 114, B08101. https://doi.org/10.1029/2008JB006002.
Jenkins, C.R., Cook, P.J., Ennis-King, J., Undershultz, J., Boreham, C., Dance, T., de Caritat, P., Etheridge, D.M., Freifeld, B.M., Hortle, A., Kirste, D., Paterson, L., Pevzner, R., Schacht, U., Sharma, S., Stalker, L., Urosevic, M., 2012. Safe storage and effective monitoring of CO2 in depleted gas fields. Proc. Natl. Acad Sci 109 (2), E35–E41.
Johnson, B.D., Boudreau, B.P., Gardiner, B.S., Maass, R., 2002. Mechanical response of sediments to bubble growth. Mar. Geol. 187, 247–363.
Johnson, B.D., Barry, M.A., Boudreau, B.P., Jumars, P.A., Dorgan, K.M., 2012. In situ tensile fracture toughness of surficial cohesive marine sediments. Geo-Marine Lett 32, 39–48. https://doi.org/10.1007/s00367-011-0243-1.
Jones, D.G., Beaubien, S.E., Blackford, J.C., Foekema, E.M., Lions, J., De Vittor, C., West, J.M., Widdicombe, S., Hauton, C., Queirós, A.M., 2015. Developments since 2005 in understanding potential environmental impacts of CO2 leakage from geological storage. Int. J. Greenh. Gas Control 40, 350–377. https://doi.org/10.1016/j.ijggc.2015.05.032.
Kallweit, R.S., Wood, L.C., 1982. The limits of resolution of zero-phase wavelets. Geophysics 47, 1035–1046.
Katsman, R., 2019. Methane Bubble Escape From Gas Horizon in Muddy Aquatic Sediment Under Periodic Wave Loading. Geophys. Res. Lett. 46, 6507–6515. https://doi.org/10.1029/2019GL083100.
Katsman, R., Ostrovsky, I., Makovsky, Y., 2013. Methane bubble growth in fine-grained muddy aquatic sediment: insight from modelling. Earth Planet. Sci. Lett. 377–378, 336–346. https://doi.org/10.1016/j.epsl.2013.07.011.
Knittel, K., Boetius, A., 2009. Anaerobic Oxidation of Methane: progress with an Unknown Process. Annu. Rev. Microbiol. 63, 311–334. https://doi.org/10.1146/annurev.micro.61.080706.093130.
Landrø, M., Wehner, D., Vedvik, N., Ringrose, P., Løhre, N.L., Berteussen, K., 2019. Gas flow through shallow sediments—a case study using passive and active seismic field data. Int. J. Greenh. Gas Control 87, 121–133. https://doi.org/10.1016/j.ijggc.2019.05.001.
Leighton, T.G., 1996. The Acoustic Bubble, (paperback edition). Academic Press, London, San Diego, p. 640 pages (ISBN 0124419216).
Leighton, T.G., Robb, G.B.N, 2008. Preliminary mapping of void fractions and sound speeds in gassy marine sediments from subbottom profiles. J Acoust Soc Am 124 (5), EL313–EL320. https://doi.org/10.1121/1.2993744 (JASA Express Letters).
Ringrose, P.S., Meckel, T.A., 2019. Maturing global CO2 storage resources on offshore continental margins to achieve 2DS emissions reductions. Sci. Rep. 9, 17944. https://doi.org/10.1038/s41598-019-54363-z.
Ruppel, C.D., Kessler, J.D., 2017. The interaction of climate change and methane hydrates. Rev. Geophys. 55, 126–168. https://doi.org/10.1002/2016RG000534.
Shell U.K Ltd., 2018. Goldeneye Pipeline Emerging Recommendation Report. In: Goldeneye Decommissioning Project, Shell Report Number GDP-PT-S-AA-7180-00002.
Sirhan, S.T., Katsman, R., Lazar, M., 2019. Methane Bubble Ascent within Fine-Grained Cohesive Aquatic Sediments: dynamics and Controlling Factors. Environ. Sci. Technol. 53, 6320–6329. https://doi.org/10.1021/acs.est.8b06848.
Strachan, N., Hoefnagels, R., Ramírez, A., van den Broek, M., Fidje, A., Espegren, K., Seljom, P., Blesl, M., Kober, T., Grohnheit, P.E., 2011. CCS in the North Sea region: a comparison on the cost-effectiveness of storing CO2 in the Utsira formation at regional and national scales. Int. J. Greenh. Gas Control 5, 1517–1532. https://doi.org/10.1016/j.ijggc.2011.08.009.
Stoker, M.S.L., D., Fyfe, J.A, 1985. A Revised Quaternary stratigraphy For the Central North Sea. HMSO, London.
Stoker, M.S., Balson, P.S., 2011. An Overview of the Lithostratigraphical Framework For the Quaternary deposits on the United Kingdom Continental Shelf. Keyworth.
Stolt, R.H., 1978. Migration by Fourior Transform. Geophysics 43, 23–48.
Taylor, P., Stahl, H., Vardy, M.E., Bull, J.M., Akhurst, M., Hauton, C., James, R.H., Lichtschlag, A., Long, D., Aleynik, D., Toberman, M., Naylor, M., Connelly, D., Smith, D., Sayer, M.D.J., Widdicombe, S., Wright, I.C., Blackford, J., 2015. A novel sub-seabed CO 2 release experiment informing monitoring and impact assessment for geological carbon storage. Int. J. Greenh. Gas Control 38, 3–17. https://doi.org/10.1016/j.ijggc.2014.09.007.
United Nations, 2015. United Nations /Framework Convention on Climate Change, Adoption of the Paris Agreement. United Nations, Paris.
Van der meer, L.G.H., 2013. The K12-B CO 2 Injection Project in the Netherlands, in: Geological Storage of Carbon Dioxide (CO2). Elsevier, pp. 301–332e. https://doi.org/10.1533/9780857097279.3.301.
Vandeweijer, V., van der Meer, B., Hofstee, C., Mulders, F., D'Hoore, D., Graven, H., 2011. Monitoring the CO2 injection site: K12-B. Energy Procedia 4, 5471–5478.
Vardy, M.E., Vanneste, M., Henstock, T.J., Clare, M.A., Forsberg, C.F., Provenzano, G., 2017. State-of-the-art remote characterization of shallow marine sediments: the road to a fully integrated solution. Near Surf. Geophys. 15, 387–402. https://doi.org/10.3997/1873-0604.2017024.
Wangen, M., Halvorsen, G., 2020. A Three-Dimensional Analytical Solution for Reservoir Expansion, Surface Uplift and Caprock Stress Due to Pressurized Reservoirs. Math. Geosci. 52, 253–284. https://doi.org/10.1007/s11004-019-09821-9.
Westergaard, H.M., 1939. Bearing pressures and cracks. J. App.l Mech. 6, A49–A53.